CANCER

Modulating tumoral exosomes and fibroblast phenotype using nanoliposomes augments cancer immunotherapy

May S. Freag[1,2], Mostafa T. Mohammed[1,3], Arpita Kulkarni[1,4], Hagar E. Emam[1], Krishna P. Maremanda[1,5], Ahmed O. Elzoghby[1]*

Cancer cells program fibroblasts into cancer associated fibroblasts (CAFs) in a two-step manner. First, cancer cells secrete exosomes to program quiescent fibroblasts into activated CAFs. Second, cancer cells maintain the CAF phenotype via activation of signal transduction pathways. We rationalized that inhibiting this two-step process can normalize CAFs into quiescent fibroblasts and augment the efficacy of immunotherapy. We show that cancer cell–targeted nanoliposomes that inhibit sequential steps of exosome biogenesis and release from lung cancer cells block the differentiation of lung fibroblasts into CAFs. In parallel, we demonstrate that CAF-targeted nanoliposomes that block two distinct nodes in fibroblast growth factor receptor (FGFR)–Wnt/β-catenin signaling pathway can reverse activate CAFs into quiescent fibroblasts. Co-administration of both nanoliposomes significantly improves the infiltration of cytotoxic T cells and enhances the antitumor efficacy of αPD-L1 in immunocompetent lung cancer–bearing mice. Simultaneously blocking the tumoral exosome-mediated activation of fibroblasts and FGFR-Wnt/β-catenin signaling constitutes a promising approach to augment immunotherapy.

INTRODUCTION

Cancer cells remodel the tumor microenvironment (TME) to evade the immune system, limiting the efficacy of cancer immunotherapy (*1*). For example, cancer cells program normal quiescent fibroblasts into a tumor-supportive myofibroblast phenotype known as cancer-associated fibroblasts (CAFs), which form the most abundant stromal cells in the TME (*2*). While normal quiescent fibroblasts exert inhibitory effect on the tumor cells, the activated CAFs suppress the immune cells and promote resistance, tumorigenesis, and metastasis (*3*). Disrupting this vicious loop between cancer cells and CAFs can potentially enhance the efficacy of cancer immunotherapy and inhibit tumor progression.

A broad range of nanomedicines have been engineered for disrupting the cross-talk between CAFs and cancer cells by different mechanisms. However, despite the central role of CAFs in tumor progression, attempts to deplete them have not translated into improved antitumor outcomes (*4*). Although targeted depletion of CAFs could relieve the stromal barrier, CAF depletion resulted in eliminating the essential extracellular matrix (ECM) components and hence disrupted the tissue homeostasis resulting in tumor hyperplasia and increased risk of metastasis. For example, the genetic deletion of α–smooth muscle actin (αSMA) + CAFs increased the infiltration of immunosuppressive regulatory T cells (T_{regs}) in the tumor, induced stemness, and ultimately led to aggressive tumor progression (*5*). Depletion of CAFs by doxorubicin or cisplatin-loaded nanoparticles induced upregulation of damage response program (DRP) molecules such as Wnt16, resulting in development of resistance (*6*). Similarly, targeting fibroblast activation protein (FAP) + CAFs with a monoclonal antibody or FAP-targeting immunotoxin led to suppression of tumor growth but failed in early phase 2 clinical trial due to limited efficacy (*7*, *8*). Therefore, the emerging paradigm is that reprogramming the CAFs into quiescent fibroblasts can better hinder tumor progression and render the tumor more responsive to treatment as opposed to deletion of CAFs (*3*, *4*). This strategy tends to keep the homeostatic role of fibroblasts while reversing their protumoral activity.

Three challenges pose a substantial barrier to reprogramming the CAFs into antitumor quiescent fibroblasts. First, new CAFs are continuously generated as the cancer cells release multiple factors that drive fibroblast programming into CAFs (*3*). Hence, to tilt the balance toward the quiescent fibroblasts, these factors need to be inhibited such that new CAFs are not generated. Second, by the time the tumor is detected, most fibroblasts have already been programmed into CAFs. These existing CAFs need to be repolarized back to a quiescent state. Third, multiple factors are involved in the above processes, introducing redundancies in the signaling pathways. These redundancies can limit the efficacy of monotherapy that target a single factor. To address the above limitations, it is therefore important to simultaneously inhibit the generation of new CAFs while inducing quiescence of the already existing ones and, rather than targeting a single factor, perturb the processes at two distinct molecular levels using rational drug combinations to overcome the redundancies.

We rationalized that cancer cell–targeted nanoliposomes that combine an exosome biogenesis inhibitor with an exosome release inhibitor can exert an effective inhibition of fibroblast programming into CAFs by cancer cells. Simultaneously, CAF-targeted nanoliposomes that combine a fibroblast growth factor receptor (FGFR) inhibitor with a downstream signal transduction inhibitor can reprogram the existing CAFs into quiescent fibroblasts. Recently, exosomes released from cancer cells were shown to deliver cytokines, DNA fragments, and coding and noncoding RNAs to the fibroblasts, triggering their differentiation into CAFs (*9*, *10*). For example, exosomal miR-1247 secreted by cancer cells was reported to induce activation of fibroblasts into myofibroblasts

[1]Division of Engineering in Medicine, Department of Medicine, Brigham and Women's Hospital, Harvard Medical School, Boston, MA, USA. [2]Investigative Toxicology, Drug Safety Research and Evaluation, Takeda Pharmaceuticals, Cambridge, MA, USA. [3]Anatomical and Clinical Pathology Department, Tufts Medical Center, Boston, MA, USA. [4]Department of Systems Biology, Harvard Medical School, Boston, MA, USA. [5]Department of Biochemistry and Biophysics, Texas A&M University, College Station, TX, USA.
*Corresponding author. Email: aelzoghby@bwh.harvard.edu

(*11*, *12*). In addition, multiple fibrogenic growth factors and mediators have been found associated with exosomal membrane including transforming growth factor–β (TGFβ), tumor necrosis factor–α (TNF-α), epidermal growth factor (EGF), FGF, and others (*10*). Compared to their soluble counterparts, exosomal proteins were reported to be more efficient in triggering differentiation of mesenchymal stem cells (MSCs) and normal fibroblasts into activated CAF phenotype. For example, the exosomal membrane-bound TGFβ induced remarkably higher fibroblast activation than identical amount of the soluble TGFβ (*9*). Therefore, we rationalized that inhibiting exosome biogenesis and release can exert a broader inhibitory effect on the cancer-mediated programming of fibroblasts over targeting a specific factor. Similarly, to maintain the activated CAF state, cancer cells secrete fibrogenic factors such as platelet-derived growth factor (PDGF) and FGF-2 (*13*). Downstream, the up-regulation of Wnt/β-catenin, Janus kinase (JAK)/signal transducer and activator of transcription (STAT), and histone deacetylase 6 (HDAC6) pathways in fibroblasts has also been found to promote and maintain the activated fibroblasts. Therefore, simultaneously inhibiting the upstream receptor and downstream nodes in the signaling pathways, i.e., blockade at two distinct levels, holds promise to reverse the activated fibroblast phenotype (Fig. 1A) (*14*).

Here, we performed a comprehensive study with a library of nanoliposomes that can perturb the above processes by inhibiting various molecular targets. We define two distinct combinations that efficiently inhibit exosome biogenesis and release and can repolarize CAFs into quiescent fibroblasts. Last, we tested the efficacy of the engineered nanoliposomes combined with anti-Programmed Death-Ligand 1 (αPD-L1) antibodies in lung cancer syngeneic mice to augment the antitumor immune response.

RESULTS

Comparative analysis of exosome biogenesis inhibitor-loaded nanoliposomes

We first validated the ability of the cancer cell–derived exosomes to induce programming of fibroblasts into CAFs. We isolated exosomes from the culture media of A549 lung cancer cells grown for 48 hours in exosome-depleted media, which were then characterized (fig. S1A), labeled using a PKH67 green fluorescent tag, and incubated with MRC5 human lung fibroblasts for another 48 hours. The exosomes were internalized into the fibroblasts (Fig. 1B and fig. S1B) and induced their differentiation into CAFs, which are characteristically larger than their quiescent counterparts and have considerably higher expression of αSMA, the classical CAFs biomarker, compared with fibroblasts incubated in culture medium without exosomes (Fig. 1B and fig. S1B).

While each of the steps involved in exosome biogenesis and release have been genetically or chemically targeted, we rationalized that nanoliposomes that exert a dual inhibition on both biogenesis and release of exosomes from cancer cells could exert a powerful inhibitory effect on the generation of CAFs (Fig. 1C). However, a comprehensive analysis comparing the impact of targeting different signaling pathways that are implicated in exosome biogenesis and release is lacking. We therefore first engineered an array of nanoliposomes with inhibitors that perturb different molecular targets implicated in either biogenesis or release of exosomes and tested them on the release of exosomes from lung cancer cells and programming of fibroblasts into CAFs (*15*–*18*). GW4869 (GW) inhibits neutral sphingomyelinase that generates ceramides, 1-phenyl-2-decanoylamino-3-morpholino-1-propanol (PDMP) inhibits glucosylceramide synthase, and tipifarnib is a farnesyltransferase inhibitor that modulates ESCRT, while NAV-2729 inhibits ADP ribosylation factor 6 (Arf6), thereby blocking exosome biogenesis. Similarly, Nexinhib20 blocks Rab27, while Shikonin (SHK) inhibits pyruvate kinase M2 (PKM2) and downstream SNAP23 (soluble NSF attachment protein 23) and SNAP receptor (SNARE) complex formation, blocking exosome release. Ketotifen, a mast cell stabilizer, is also known to inhibit exosome release, while calpeptin perturbs the cytoskeletal structures that underlie multivesicular bodies (MVBs) trafficking. We incorporated these inhibitors into nanoliposomes, which were engineered via thin-film hydration followed by extrusion through 200-nm porous membranes. Other than PDMP and NAV-2729, which failed to form stable nanoliposomes (and hence not studied further), the others resulted in stable nanoliposomes between 90 and 170 nm and low polydispersity (table S1 and fig. S2).

We next treated human A549 lung cancer cells with the different nanoliposomes and quantified the release of exosomes. Compared to the control nontreated cancer cells, all the nanoliposomes significantly reduced the release of exosomes from cancer cells to different extents as shown by reduction of total protein content measured using Bicinchoninic Acid (BCA) protein assay (Fig. 1D). More specifically, we quantified the isolated exosomes based on their expression of the surface tetraspanin marker molecule CD63 using ExoELISA assay kits (*19*). The concentration of the $CD63^+$ exosomes released from A549 cells was significantly reduced from 9.41×10^{10} particles/ml in control A549 cells to a range of 1.5×10^{10} to 3.4×10^{9} particles/ml following treatment of the cells with the nanoliposomes (Fig. 1D). We next validated the number of harvested exosomes from cancer cells by measuring the enzymatic activity of the exosomal acetylcholinesterase, known to be enriched in the exosomal membrane, using an EXOCET colorimetric assay (*20*). The nanoliposome-treated cancer cells released a significantly lower number of exosomes compared to the nontreated cancer cells (controls) (Fig. 1D). To further validate these observations across exosome heterogeneity, we used an interferometric imaging technique to count individual exosomes and fractionate populations of exosomes that exhibit specific surface proteins (*21*, *22*). This confirmed the inhibitory effect of our nanoliposomes on the release of various populations of exosomes ($CD63^+$, $CD81^+$, $CD9^+$, and $EpCAM^+$) from A549 cancer cells compared to the nontreated cells (fig. S3, A to F). The data from label-free interferometric analysis confirmed that the nontreated cells released 2- to 2.5-fold more exosomes, particularly $CD9^+$ exosomes, than the nanoliposome-treated cells, while GW-treated cells released the fewest number of exosomes.

We next tested the impact of treatment of cancer cells with the exosome release inhibitory nanoliposomes on programming of fibroblasts into CAFs. We directly cocultured growth-arrested MRC5 fibroblasts with exosomes isolated from A549 cells that were treated with the above nanoliposomes (Fig. 1E). Treatment of cancer cells with the nanoliposomes resulted in significantly lower degree of fibroblast activation quantified by both flow cytometry and immunofluorescence imaging for the CAFs biomarker αSMA (Fig. 1, F to H) and fibronectin (fig. S4). We additionally validated these observations in a murine Lewis lung cancer (LLC) cell line. Treatment of LLCs with the nanoliposomes significantly decreased exosome release and programming of murine NIH3T3 fibroblasts into CAFs (fig. S5). Together, these studies show SHK- and GW-loaded nanoliposomes resulted in numerically greatest reduction of exosome release from lung cancer cells, whereas tipifarnib and calpeptin exhibited the lowest inhibitory effect on exosome release.

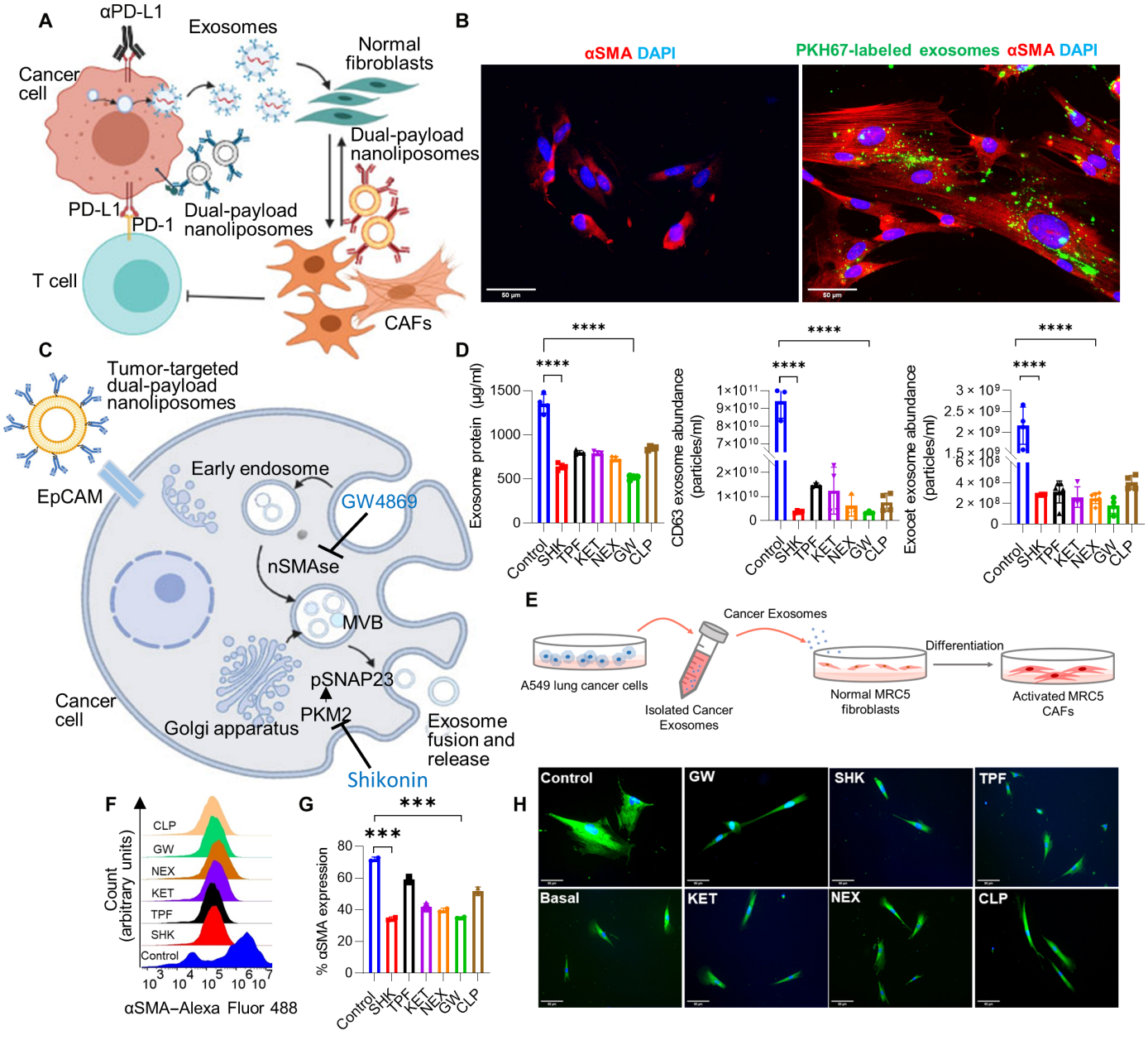

Fig. 1. Mechanistically inspired nanoliposomes remodel CAFs. (**A**) Tumor-targeted nanoliposomes enter lung cancer cells via binding to EpCAM and release their cargo to inhibit exosome biogenesis and release. In parallel, GPR77/CD10-targeted nanoliposomes allow selective targeting of CAFs, where the incorporated drugs reverse activated CAFs into quiescence. The combined nanoliposome-mediated normalization of CAFs blocks their immunosuppressive activity and augment αPD-L1 immunotherapy. (**B**) Immunofluorescence images show MRC5 human lung fibroblasts cultured for 48 hours without exosomes (left) and its activation into CAFs when cocultured with A549 cancer cell–derived PKH67-labeled exosomes for 48 hours (right) followed by staining with anti-αSMA antibody. Scale bars, 50 μm. (**C**) GW and SHK inhibit two consecutive steps in biogenesis and release of exosomes from a cancer cell. GW inhibits neutral sphingomyelinase enzyme (nSMase) to prevent inward budding of ceramide into intraluminal vesicles, while SHK blocks PKM2-mediated phosphorylation of SNAP23 to prevent SNARE complex formation and exocytosis, respectively. (**D**) Graphs show the effect of nanoliposomes on release of cancer-derived exosomes, quantified using BCA standard protein assay, CD63 ExoELISA, and EXOCET assay. A549 cancer cells were treated with nanoliposomes containing different exosome biogenesis inhibitors for 24 hours. Data shown are means ± SE [n = 3 to 4, ****$P < 0.0001$, analysis of variance (ANOVA) followed by Bonferroni's post hoc test]. (**E**) A549 cancer cells were treated with nanoliposomes, and the released exosomes were cultured with MRC5 fibroblasts for 48 hours. (**F**) Flow cytometric analysis shows the effect of nanoliposomes on αSMA expression in MRC5 fibroblasts cultured with exosomes isolated from treated cancer cells. (**G**) Graph shows the quantified αSMA expression in MRC5 fibroblasts. Data shown are means ± SE (n = 2, ***$P < 0.001$, ANOVA with Bonferroni's post hoc test). (**H**) Immunofluorescence imaging for αSMA in MRC5 fibroblasts cultured with nanoliposome-treated A549 cancer cell–derived exosomes for 48 hours. Scale bar, 50 μm. DAPI, 4′,6-diamidino-2-phenylindole; MVB, multivesicular body.

Suppression of exosome release from lung cancer cells using SHK/GW nanoliposomes

As GW and SHK inhibit the sequential steps of biogenesis and release of exosomes, respectively, we rationalized that nanoliposomes that combine both these molecular therapeutics would exert optimal efficacy in reducing exosome-mediated activation of fibroblasts into CAFs. We therefore engineered nanoliposomes with three different molar ratios (1:1, 1:5, and 1:10 SHK/GW ratios). Coupling of antibodies on the surface of nanoliposomes has been shown to enhance tumor targeting and improve antitumor efficacy (Fig. 2A). We therefore coupled anti–Epithelial Cell Adhesion Molecule (EpCAM) antibodies to the surface of the nanoliposomes through the carboxylic group of 1,2-distearoyl-sn-glycero-3-phosphoethanolamine-N-[carboxy(polyethylene glycol)-2000] (DSPE-PEG). The nanoliposomes ranged between 90 and 140 nm in diameter and were stable over time (Fig. 2, B to D, and table S2). As the 1:10 ratio of SHK to GW resulted in optimal size of 93.89 nm, and additionally at all three ratio, the nanoliposomes exhibited a similar concentration-dependent cytotoxicity against lung cancer cells (Fig. 2E and fig. S6A), we selected the 1:10 SHK/GW drug ratio for further studies. Both drugs exhibited high-loading efficiency and were released from the nanocarrier in a sustained rate (Fig. 2, F and G). We used the drug nanoliposomes at a concentration corresponding to 1 μM SHK and 10 μM GW, lower than its IC_{50} (median inhibitory concentration) (5 and 10 μM, respectively), to dissect the impact on the release of exosomes with limited confounding effect from cell death. Increasing the anti-EpCAM antibody concentration resulted in increased binding to A549 cancer cells from 41.6 to 72% as demonstrated by flow cytometry analysis. Furthermore, the EpCAM-targeted nanoliposomes demonstrated higher internalization into the cells compared to nontargeted ones as evidenced by fluorescence microscopy (Fig. 2, H and I, and figs. S6B and S7). We next confirmed the inhibitory effect of the combined nanoliposomes on exosome release by nanoparticle tracking analysis (NTA). NTA demonstrated a high concentration of the nontreated cancer cell–derived exosomes (5.4×10^{10} particles/ml), which was reduced by 4.7-, 7.4-, and 9.9-folds upon treatment of cells with SHK, GW, and SHK-GW nanoliposomes, respectively (Fig. 2, J and K). This was validated via flow cytometry using CD9 anti-tetraspanin antibody-coated magnetic microbeads for immunocapturing of exosomes (Fig. 2, L and M, and fig. S8), CD81/CD63 anti-tetraspanin antibody-coated beads (figs. S9 and S10), BCA protein assay (Fig. 2N), CD63 ExoELISA assay (Fig. 2O), and EXOCET cholinesterase assay (Fig. 2P). A similar observation was made in LLC cells, where the combined nanoliposomes exerted a greater inhibition than either drug nanoliposomes alone (Fig. 2Q).

Reducing fibroblast activation using EpCAM-targeted SHK/GW nanoliposomes

We next tested the ability of the EpCAM-targeted SHK/GW nanoliposome-treated cancer cells to program fibroblasts into CAFs. We treated the A549 lung cancer cells with the nanoliposomes for 24 hours and then indirectly cocultured with MRC5 fibroblasts via a Transwell system that allows the transfer of exosomes to the fibroblasts (Fig. 3A). The fibroblasts cocultured with the nontreated cancer cells were highly activated and differentiated into CAFs with characteristic striated morphology of large bundles of microfilaments. On the other hand, treatment of cancer cells with the SHK/GW nanoliposomes inhibited the activation of fibroblasts as evidenced by remarkable phenotypic difference from the activated CAFs with no striations and the decreased expression of all CAFs markers and ECM proteins as revealed by immunostaining (Fig. 3B) and flow cytometry (Fig. 3C). Flow cytometry revealed that the treatment of A549 cancer cells by the SHK/GW nanoliposomes reduced the expression of αSMA and Collagen Type I Alpha 1 (COL1A1) in fibroblasts by 2.8- and 2.95-folds, respectively, compared to activated CAFs cocultured with nontreated cancer cells. Similarly, the expression of FAP, S100A4, and fibronectin in normalized fibroblasts was reduced by 1.4-, 1.3-, and 1.6-folds, respectively. These results were further validated using additional two experimental setups that did not include a Transwell system. In the first model, MRC5 fibroblasts were treated with the conditioned media (CM) of A549 cells pretreated with the SHK/GW nanoliposomes, while in the second model, the A549 cells were directly cocultured with MRC5 fibroblasts and then were treated with the SHK/GW nanoliposomes for 24 hours followed by further 48-hour coculture. In both models, the drug treatment inhibited fibroblast activation with reduced expression of both αSMA and COL1A1 (Fig. 3, D and E). Similar results were obtained using indirect Transwell coculture of murine lung cancer LLC cells/murine NIH3T3 fibroblasts and human HT29 colon cancer cells/CCD-18Co colon fibroblasts (fig. S11).

Mechanistically, GW, a neutral sphingomyelinase 2 inhibitor, prevents the formation of MVBs by inhibiting the inward budding of ceramide, while SHK, PKM2 inhibitor, inhibits the phosphorylation of SNAP23, thus preventing the formation of SNAREs complex involved in membrane docking and release of exosomes. As shown in fig. S12, immunostaining the SHK/GW nanoliposome-treated A549 cells for pPKM2, pSNAP23, and ceramide showed a reduced expression compared to the nontreated cells. In addition, quantitative reverse transcription polymerase chain reaction (qRT-PCR) analysis of the MRC5 fibroblasts indirectly cocultured with SHK/GW nanoliposome-treated A549 cancer cells showed down-regulation of *CCNA2* proliferation gene (Fig. 3F). Silencing of *CCNA2* gene was reported to inhibit cell proliferation, migration, and invasion (*23*, *24*). In addition, our treatment resulted in down-regulation of both *interleukin-6* (*IL-6*) and *TNF*α, two inflammatory cytokines that markedly contribute to CAF-mediated immunosuppression, tumorigenesis, metastasis, and drug resistance (*25*, *26*). Up-regulation of the stemness marker SRY-box transcription factor 2 (*SOX2*) in CAFs was found to promote CAF-activated phenotype and enhance tumorigenesis (*27*). *CD44* overexpressed by CAFs also contributes to cancer stemness and drug resistance (*28*). Both biomarkers were down-regulated in fibroblasts after treatment of cancer cells with SHK/GW nanoliposomes (Fig. 3F). Collectively, inhibition of exosome-mediated activation of fibroblasts reduced the expression of genes responsible for proliferation, immunosuppression, cancer stemness, and drug resistance.

Halting CAF programing to dampen their tumorigenic and immunosuppressive functions

We evaluated the secretory profiles of CAFs cocultured in the Transwells with A549 cancer cells pretreated with the nanoliposomes. Tumoral TGFβ1 expressed at exosomal membrane constitutes 53.4 to 86.3% of the total TGFβ1 secreted by cancer cell and is reported to be one of the key drivers of fibroblast activation through the stimulation of SMAD pathway (*29*). The cancer-derived exosomal TGFβ1 is mainly responsible for fibroblast differentiation into the tumor-promoting CAFs, which, in turn, secretes TGFβ1 that induce an immunosuppressive TME. The levels of TGFβ1 were reduced by ninefold upon treatment with the combined SHK/GW nanoliposomes (Fig. 3G). TGFβ1 is also reported to increase the production of fibroblast FGF2, which, in turn, binds to FGFR to promote tumor growth, migration,

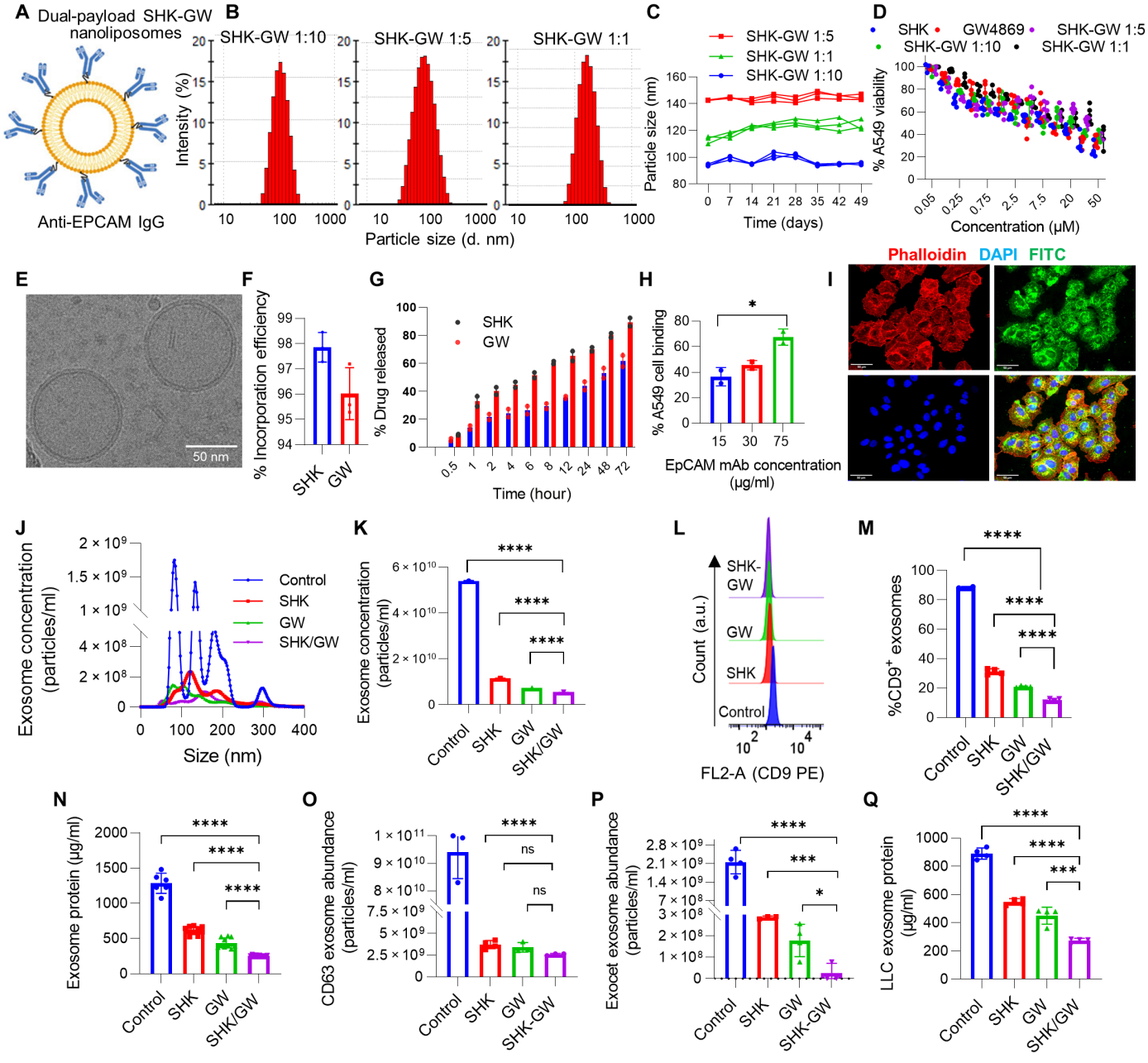

Fig. 2. Tumor-targeted dual drug-loaded nanoliposomes decrease exosome load. (**A**) Schematic shows EpCAM antibody–coupled nanoliposomes coloaded with SHK and GW4869. (**B**) Effect of drug molar ratio on nanoliposome size. (**C**) Hydrodynamic diameter of SHK/GW nanoliposomes upon storage at 4°C as a measure of stability. (**D**) CCK8 viability assay of A549 cancer cells treated with nanoliposomes for 24 hours at 37°C CO_2 incubator. (**E**) Cryo–transmission electron microscopy (cryo-TEM) image of nanoliposomes. (**F**) Drug incorporation and (**G**) release from nanoliposomes in PBS pH 7.4 at 37°C. Data shown are means ± SE ($n = 2$). (**H**) Binding of EpCAM-targeted fluorescein isothiocyanate (FITC)–loaded nanoliposomes after incubation with A549 lung cancer cells for 4 hours at 4°C analyzed by flow cytometry. (**I**) Fluorescence imaging shows internalization of EpCAM-targeted FITC-loaded nanoliposomes into A549 cancer cells after their coculture for 24 hours at 37°C CO_2 incubator. Scale bar, 50 μm. (**J** and **K**) NTA of exosomes isolated from A549 cancer cells treated with SHK/GW nanoliposomes. Graph shows means ± SD ($n = 3$, $^{****}P < 0.0001$, ANOVA followed by Bonferroni's post hoc test). (**L**) CD9 EXO-Flow cytometry of A549 exosomes immunocaptured on CD9 antibody–coated magnetic microbeads, followed by staining with phycoerythrin-conjugated fluorescent antibody. (**M**) Graph shows means ± SD ($n = 2$ to 4, $^{****}P < 0.0001$, ANOVA followed by Bonferroni's post hoc test). Quantification of A549 exosomes after treatment with SHK/GW nanoliposomes via (**N**) BCA protein assay. Data shown are means ± SD ($n = 6$ to 10, $^{****}P < 0.0001$, ANOVA followed by Bonferroni's post hoc test) and (**O**) CD63 Exo-ELISA assay. Data shown are means ± SD ($n = 3$ to 4, $^{****}P < 0.0001$, ANOVA followed by Bonferroni's post hoc test). (**P**) EXOCET cholinesterase assay. Data shown are means ± SD ($n = 3$ to 4, $^{*}P < 0.05$, $^{***}P < 0.001$, and $^{****}P < 0.0001$, ANOVA followed by Bonferroni's post hoc test). (**Q**) Quantification of exosomes isolated from LLC cells treated with SHK/GW nanoliposomes via BCA protein assay. Data shown are means ± SD ($n = 6$ to 10, $^{****}P < 0.0001$, ANOVA followed by Bonferroni's post hoc test). IgG, immunoglobulin G; a.u., arbitrary units; ns. not significant.

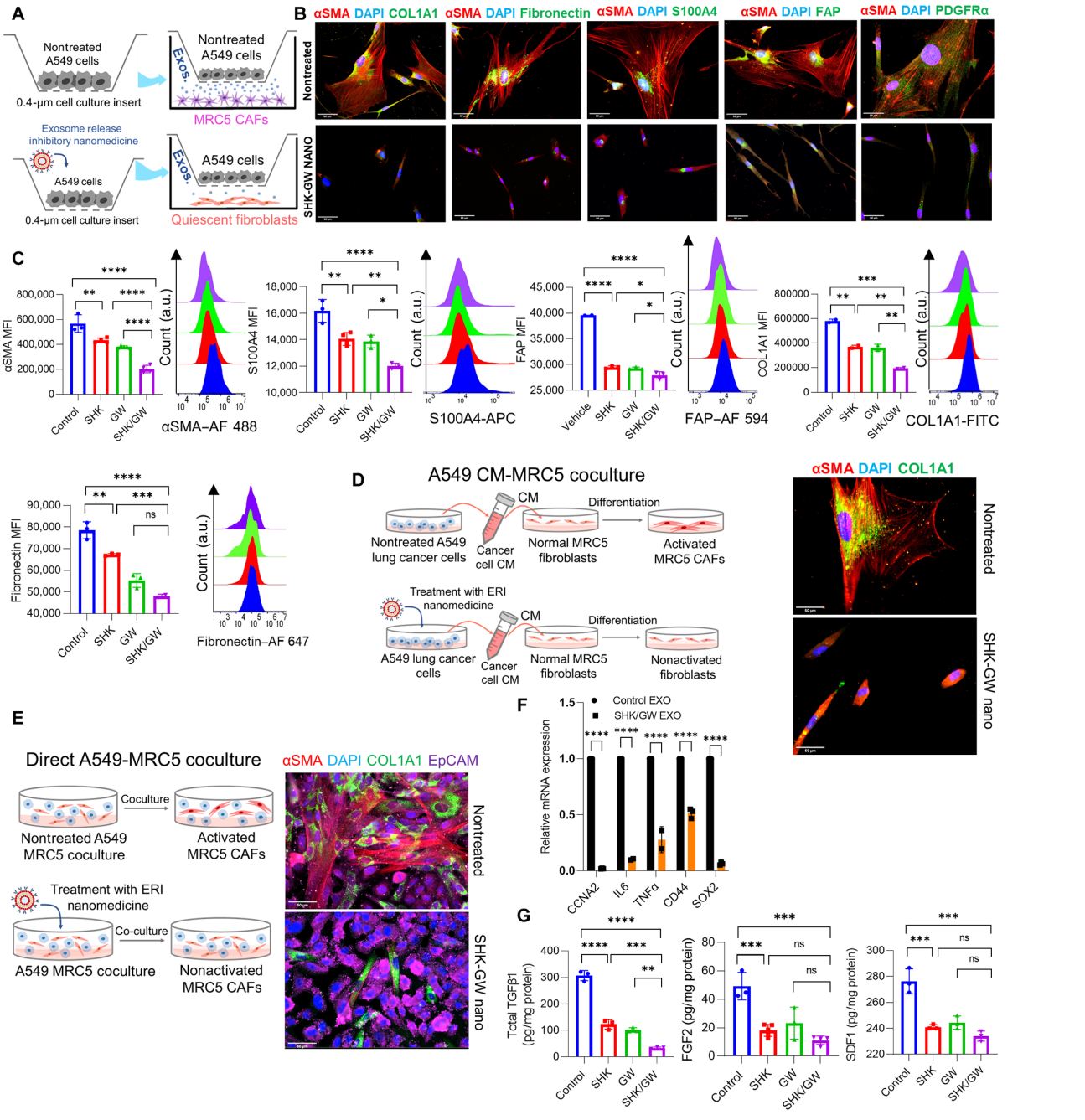

Fig. 3. Exosome release inhibitory nanoliposomes block CAF generation. (**A**) Indirect coculture of A549 lung cancer cells cultured on the top chamber of 0.4-μm transwell and MRC5 lung fibroblasts cultured on the bottom chamber. Top: Nontreated A549 cells. Bottom: A549 cells pretreated with EpCAM-targeted SHK/GW nanoliposomes for 24 hours. (**B**) Immunofluorescence imaging of fibroblast and ECM activation markers in MRC5 fibroblasts indirectly cocultured for 48 hours with A549 cancer cells pretreated with SHK/GW nanoliposomes. Scale bars, 50 μm. (**C**) Flow cytometry analysis of the expression of fibroblast and ECM activation markers in MRC5 fibroblasts indirectly cocultured for 48 hours with A549 cancer cells pretreated with SHK/GW nanoliposomes. Graphs show means ± SD ($n = 2$ to 5, $^{*}P < 0.05$, $^{**}P < 0.01$, $^{***}P < 0.001$, and $^{****}P < 0.0001$, ANOVA followed by Bonferroni's post hoc test). (**D**) MRC5 fibroblasts cocultured for 48 hours with CM of A549 cancer cells pretreated with SHK/GW nanoliposomes followed by fluorescence microscopy. Scale bar, 50 μm. (**E**) MRC5 fibroblasts directly cocultured with A549 cancer cells at 1:1 ratio and then treated with SHK/GW nanoliposomes for 24 hours. The medium was then replaced with fresh medium supplemented in 5% exosome-depleted FBS for 48 hours, followed by fluorescence microscopy. Scale bar, 50 μm. (**F**) Relative mRNA expression of MRC5 fibroblasts indirectly cocultured for 48 hours with A549 cancer cells pretreated with SHK/GW nanoliposomes for 24 hours, followed by qRT-PCR analysis. Data are shown as means ± SD ($n = 2$ to 5, $^{****}P < 0.0001$, ANOVA followed by Bonferroni's post hoc test). (**G**) Secretory ELISA profile of MRC5 fibroblasts indirectly cocultured for 48 hours with A549 cancer cells pretreated with SHK/GW nanoliposomes for 24 hours. Graphs show means ± SD ($n = 2$ to 5, $^{**}P < 0.01$, $^{***}P < 0.001$, and $^{****}P < 0.0001$, ANOVA followed by Bonferroni's post hoc test). MFI, mean fluorescence intensity. IFN-γ, inteferon-γ.

and angiogenesis (*10*). We observed a decrease in secreted FGF2 from 49.2 to 11.2 pg/mg protein when treated with the SHK/GW nanoliposomes (Fig. 3G). CAFs are the main source of CXCL12 (SDF-1) in TME. CXCL12 binds to CXCR4 and CXCR7 in TME, which enhances cancer cell migration and growth and contributes to development of resistance to immune checkpoint inhibitors (ICIs) (*30*, *31*). In addition, as an autocrine function, CXCL12 maintains the tumorigenic CAF phenotypes. Therefore, reducing the secretion of CXCL12 can reverse the immunosuppressive TME and maintains the quiescent fibroblasts. In our study, treating the cancer cells with the SHK/GW nanoliposomes reduced the secretion of SDF-1 from CAFs by 1.2-fold compared to CAFs cocultured with nontreated cancer cells (Fig. 3G).

Subsequently, we tested if normalization of fibroblast can weaken the cross-talk with cancer cells. In a scratch assay, we found that treatment of A549 cancer cells with CM of the activated CAFs significantly accelerated their migration (~527.3 μm) compared to when cultured in control media (~127.3 μm) or with media from quiescent fibroblasts cocultured with cancer cells treated with the dual drug nanoliposomes (~178.2 μm) (Fig. 4, A to C). Similarly, the CM from activated CAFs increased the invasive properties of A549 cancer cells in collagen-coated Transwell coculture test. This invasive behavior was inhibited when the cancer cells were cultured with CM from normalized fibroblasts (Fig. 4, D to F). We also evaluated the effect of fibroblast normalization on the polarization status of macrophages (*32*). Activated CAFs were generated by coculturing with cancer cell–derived exosomes. Treatment of phorbol 12-myristate 13-acetate (PMA)–pretreated THP-1 macrophages with the CM of activated CAFs enhanced their polarization into M2 phenotype where the cells became more elongated and spindle shaped with higher expression of the M2 markers Arginase 1 and CD163. In contrast, the coculture of PMA-pretreated THP-1 macrophages with the CM of fibroblasts, cultured with cancer cells treated with the SHK/GW nanoliposomes, increased their M1 polarization with the cells became dendritic-like with filopodia or cytoplasmic extrusions and with higher expression of the M1 markers TNFα and CD86 resulting in threefold higher M1/M2 ratio compared to cells treated with activated CAF CM (Fig. 4, G to J, and fig. S13). Similar results were previously obtained where pancreatic CAFs that promoted polarization of monocytes to M2 phenotype by secreting macrophage colony-stimulating factor and increasing reactive oxygen species (ROS) production in monocytes (*33*). Last, we tested the effect of CAF phenotype programming on the activity of cytotoxic T cells. Treatment of splenic $CD8^+$ T cells with CM of normalized CAFs resulted in significant up-regulation of the expression of some key genes essential for the cytotoxic activity of T cells, including *perforin* (2.6-), *granzyme B* (13.2-), and *interferon*-γ (2.2-folds) (Fig. 4, K and L). Several studies have reported the ability of CAFs to impair the activity and proliferation of effector $CD8^+$ T cells by secreting different factors such as TGF-β1, Arginase 2, Indoleamine 2,3-dioxygenase 1 (IDO1), and galectin-1 (*26*, *34*).

Screening the potential of FGFR inhibitors to reverse the activated CAFs phenotype

We rationalized that the pre-existing CAFs can be reprogrammed into quiescent fibroblasts using nanoliposomes that perturb the signaling loops that maintain the activated CAF phenotypic state. FGF, which is elevated in the coculture of cancer cells and fibroblasts as seen earlier, stimulates key signaling pathways in CAFs to maintain their activated phenotype (*35*). We therefore engineered a comprehensive array of nanoliposomes using thin-film hydration followed by extrusion as described earlier, incorporating FGFR inhibitors (e.g. nintedanib, erdafitinib, pemigatinib, fisogatinib, TAS-120, H3B-6527, and BGJ398) (*36*, *37*) or downstream signal transduction inhibitors including JAK2/STAT inhibitor (e.g., AG-490) (*38*), Wnt/β-catenin inhibitor (e.g., ICG-001) (*39*), Twist1 inhibitor (e.g., Harmine) (*40*, *41*), and HDAC6 inhibitor (e.g., CAY10603) (*42*) (Fig. 5A, table S3, and fig. S14).

We next screened these nanoliposomes for their ability to reverse TGFβ1-activated MRC5 fibroblasts to a quiescent state at concentrations used in previous studies (Fig. 5B). Among the tested nanoliposomes with FGFR inhibitors, TAS-120 showed the most efficient phenotype reversal of TGFβ1-preactivated MRC5 and NIH3T3 fibroblasts quantified as decrease in fluorescence intensity of αSMA (Fig. 5C and figs. S15 and S16) and significant reduction of expression of CAF markers (αSMA and FAP) and ECM proteins (COL1A1 and fibronectin) measured by flow cytometry (Fig. 5D and figs. S15B and S16). Harmine-loaded nanoliposomes resulted in considerable apoptosis of fibroblasts, while ICG-001–, CAY10603-, and AG490-loaded nanoliposomes successfully reversed the activated phenotype of TGFβ1-preactivated fibroblasts. The Wnt/β-catenin inhibitor, ICG-001, was found to be most effective downstream molecular-targeted inhibitor in reversing the activated CAF phenotype (Fig. 5E and figs. S15 and S16B).

Targeting nanoliposomes to stemness-promoting CAFs

Targeting a specific subset of CAFs fostering immunosuppression and promoting tumor growth rather than targeting heterogenous CAF populations remains an unmet need. Recently, CD10, a zinc-dependent metalloproteinase (*43*, *44*), and G protein–coupled receptor 77 (GPR77) (*45*, *46*), an alternative receptor for complement C5a, were identified as highly specific surface markers for protumorigenic CAFs and strongly related to resistance of CAFs to chemotherapy (*3*). $GPR77^+CD10^+$ CAFs have been found to enrich cancer stem cells (CSCs) by secreting prostemness factors IL-6 and IL-8, which are also known by their immune-suppressive effects (*43*, *47*–*49*). Breast cancer and non–small cell lung cancer (NSCLC) patients with higher numbers of $GPR77^+CD10^+$ CAFs in tumors exhibited shorter survival, and those CAFs were observed surrounding CSCs in the clinical tumor samples (*43*).

Therefore, we developed nanoliposomes targeting $GPR77^+CD10^+$ CAFs based on their reported role in promoting tumor growth and drug resistance (*43*). We observed the concentration-dependent binding of antibodies against CD10 and GPR77 on MRC5 cultured in CM of A549 cells (fig. S17, A and B). Engineering the nanoliposomes with increasing concentrations of the antibodies on their surface increased their MRC5 cell binding in a linear pattern (Fig. 5, F and G). CAFs exhibit remarkable heterogeneity (*3*). For example, a dual $CD10^+GPR77^+$ CAF comprised more than 70% of the total CAFs in a drug-resistant tumor (*43*). There are CAFs that express CD10 but low levels of GPR77 and vice versa (*43*). We therefore rationalized that nanoliposomes that displayed antibodies against both GPR77 and CD10 should specifically target the desired CAFs population. The dual GPR77/CD10 (1:1 ratio)–targeted nanoliposomes showed significantly higher binding to CAFs compared to single CD10- or GPR77-targeted nanoliposomes by 1.4- and 1.9-folds, respectively (Fig. 5H) and resulted in the higher internalization of nanoliposomes into MRC5 CAFs compared to nontargeted nanoliposomes (Fig. 5I and fig. S17C).

A GPR77/CD10-targeted dual drug nanoliposomes for CAF reprograming. Pharmacologically, the inhibition of signaling pathways

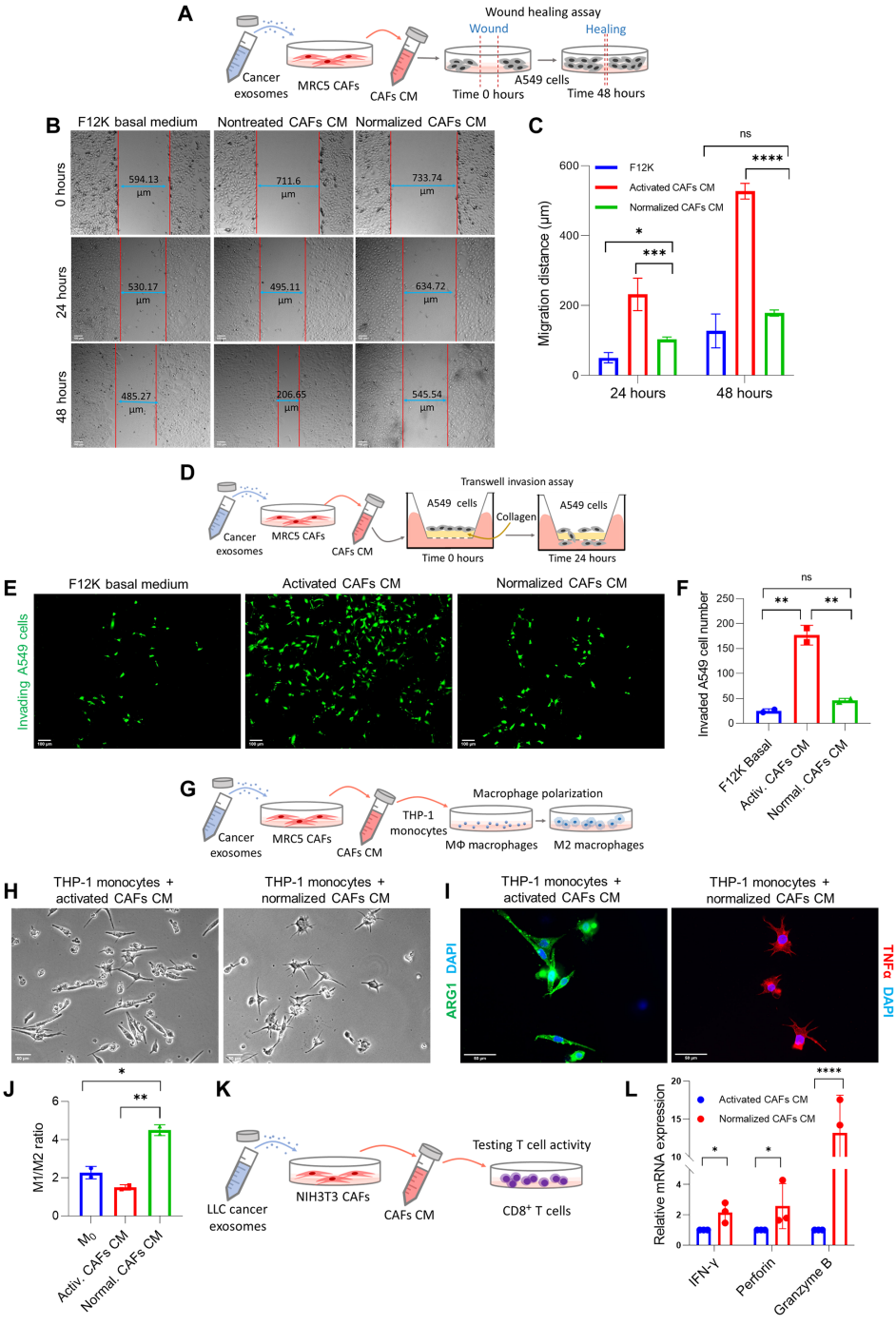

Fig. 4. Effect of fibroblast phenotype on behavior of cancer and immune cells. (**A**) Wound healing assay for testing the migration of A549 cancer cells treated with CM of activated and normalized CAFs. (**B**) Bright-field images of the wound before and after treatment with each CAF CM. Scale bars, 100 µm. (**C**) Quantification of migration distance calculated from the width of wound measured at 0-, 24-, and 48-hour time points. Graphs show means ± SD ($n = 3$, $^*P < 0.05$, $^{***}P < 0.001$, and $^{****}P < 0.0001$, ANOVA followed by Bonferroni's post hoc test). (**D**) Transwell invasion assay for evaluating the invasion of A549 cancer cells seeded into a collagen-coated transwell chamber and allowed to invade toward CM of activated and normalized CAFs in the lower chamber for 24 hours. (**E**) Fluorescence microscope images and (**F**) Quantification of the invading A549 cells stained with calcein AM. Scale bars, 100 µm. Graphs show means ± SD ($n = 2$ to 3, $^{**}P < 0.01$, ANOVA followed by Bonferroni's post hoc test). (**G**) Schematic showing coculture of THP-1 macrophages with CM of CAFs. (**H**) Bright-field and (**I**) immunofluorescence imaging of THP-1 monocytes pretreated with PMA (25 ng/ml) for 24 hours and then treated with CM of activated (left) or normalized CAFs (right) for 48 hours. Scale bars, 50 µm. (**J**) M1/M2 macrophage polarization ratio calculated from the expression of Arginase/TNFα analyzed by flow cytometry. Graph shows means ± SD ($n = 2$, $^*P < 0.05$ and $^{**}P < 0.01$, ANOVA followed by Bonferroni's post hoc test). (**K**) Schematic showing coculture of $CD8^+$ T cells isolated from mouse splenocytes by negative selection with CM of activated and normalized CAFs for 48 hours. (**L**) Analysis of mRNA expression of the harvested T cells via qRT-PCR. Graph shows means ± SD ($n = 3$, $^*P < 0.05$ and $^{****}P < 0.0001$, ANOVA followed by Bonferroni's post hoc test).

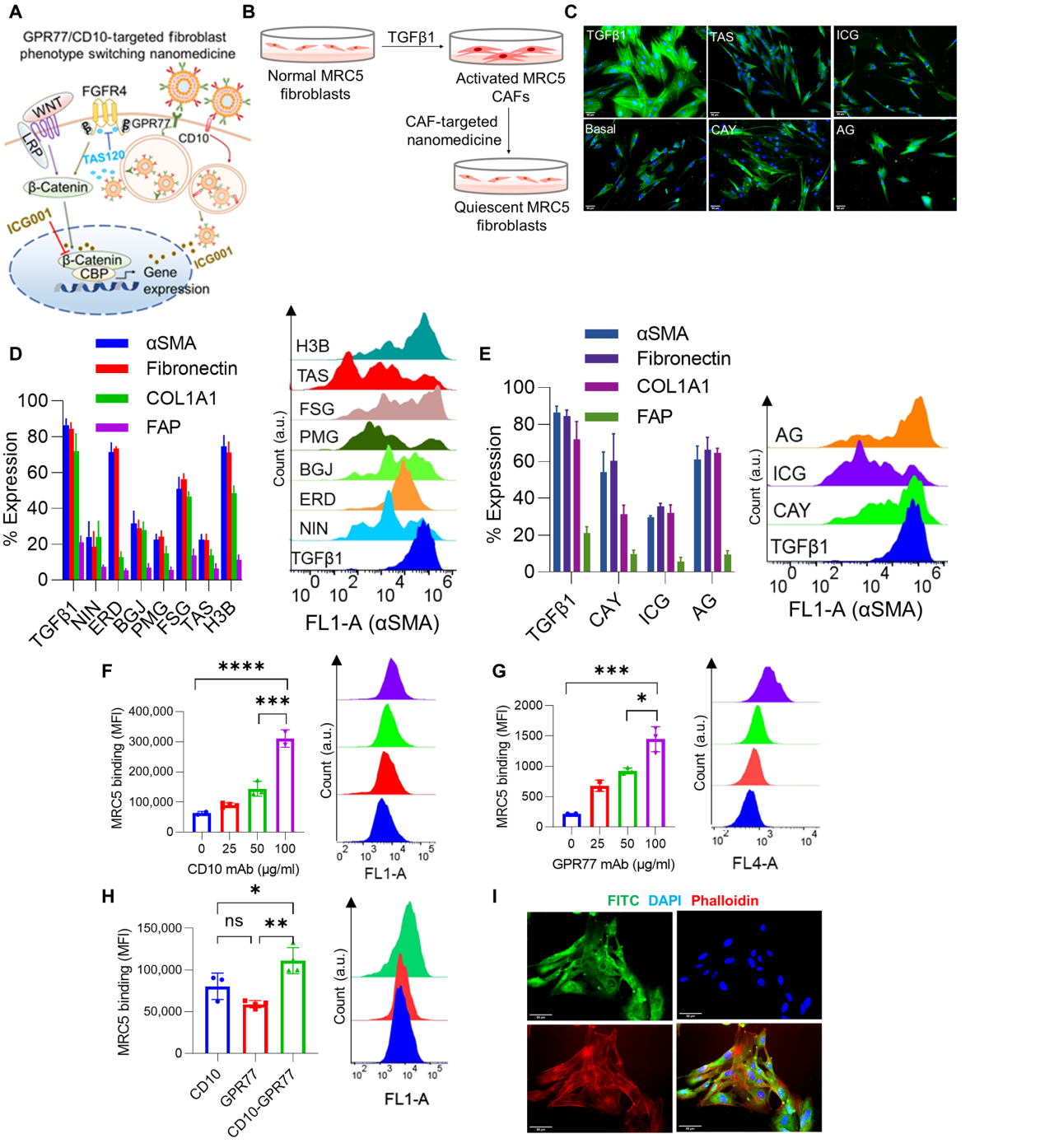

Fig. 5. Targeting signaling pathways switches CAFs into a quiescent phenotype. (**A**) Schematic shows that GPR77/CD10-targeted nanoliposomes allow selective targeting of CAFs. The nanoliposomes were internalized into CAFs via binding to the overexpressed proteins GPR77 and CD10 and then releases inhibitors of FGFR and Wnt/β-catenin signaling pathways; TAS-120 and ICG-001, respectively, to synergistically induce reversal of the activated phenotype of CAFs into a quiescent one. (**B**) Preactivation of MRC5 lung fibroblasts into CAFs via treatment with TGFβ1 (10 ng/ml) for 24 hours then treated with CAF-targeted drug nanoliposomes for 24 hours for initial screening. (**C**) Immunofluorescence imaging of MRC5 lung fibroblasts preactivated using TGFβ1 (10 ng/ml) for 24 hours and then treated with CAF-targeted nanoliposomes followed by fluorescence microscopy. Scale bars, 50 μm. Flow cytometry analysis of fibroblast activation markers and ECM markers in TGFβ1 preactivated MRC5 fibroblasts after treatment with (**D**) FGFR inhibitors and (**E**) downstream signal transduction inhibitors. Flow cytometry analysis of the binding of (**F**) single CD10, (**G**) single GPR77, and (**H**) dual GPR77/CD10-targeted nanoliposomes after incubation of antibody-coupled nanoliposomes with A549 CM-preactivated MRC5 fibroblasts for 4 hours at 4°C. Data are shown as means ± SD ($n = 3$, $^*P < 0.05$, $^{****}P < 0.0001$, ANOVA followed by Bonferroni's post hoc test). (**I**) Fluorescence imaging of the internalization of dual GPR77/CD10-targeted FITC-loaded nanoliposomes into MRC5 lung fibroblasts after incubation for 24 hours at 37°C CO_2 incubator followed by fluorescence microscopy. Scale bars, 50 μm. mAb, monoclonal antibody.

at distinct loci results in increased efficacy (*50*). On the basis of the above findings, we next engineered dual-payload nanoliposomes combining TAS + ICG, TAS + AG, and TAS + CAY. Treatment of TGFβ1-activated fibroblasts with the TAS/ICG nanoliposomes for 24 hours resulted in the maximal reduction in the expression of CAF biomarkers, αSMA, S100A4, COL1A1, and fibronectin, compared with the other combinatorial nanoliposomes or to a single payload TAS nanoliposomes (Fig. 6, A to E, and fig. S18). All treatments resulted in significant reduction in secreted TGFβ1, CXCL12, and FGF2 compared with nontreated CAFs (Fig. 6, F to H). The nanoliposomes formed were stable, had >95% loading efficiency for both drugs, a size range of 140 to 155 nm, and a polydispersity index of <0.2 (Fig. 6I, table S4, and fig. S14). As the TAS + ICG emerged as the most effective combination nanoliposomes to induce quiescence of the activated CAFs phenotype, we selected this combination for further studies.

A GPR77/CD10-targeted nanoliposomes coloaded with ICG-001 and TAS-120 showed a size of ~153.7 nm and a surface charge of −44.6 mV, with optimal drug loading and release over 72 hours (Fig. 6, J to N). The GPR77/CD10-targeted nanoliposomes coloaded with ICG-001 and TAS-120 exhibited similar cell viability as ICG- or TAS-loaded nanoliposomes (Fig. 6O). Our nanoliposome treatment resulted in substantial induction of quiescent fibroblast phenotype as reflected by remarkable up-regulation of three quiescence genes *CDKN1A* (encoding p21), *CDKN1B* (encoding p27), and *ENTPD1* (CD39) compared to the nontreated CAFs, which in turn triggers cell cycle quiescence (Fig. 6P) (*51*, *52*). Furthermore, qRT-PCR analysis of the TAS/ICG nanoliposome-treated TGFβ1-preactivated MRC5 fibroblasts showed down-regulation of *CCNA2*, *IL-6*, *TNF*α, and *CD44* responsible for the activation, tumorigenic, immunosuppressive, and stemness of CAFs compared to the nontreated ones (Fig. 6Q) (*53*). After activation of MRC5 fibroblasts by TGFβ1 for 24 hours, treatment with GPR77/CD10-targeted TAS/ICG nanoliposomes for 24 hours reversed the phenotype of activated fibroblasts as shown by reduction in the fluorescence intensity of αSMA, COL1A1, fibronectin, FAP, and S100A4 compared to control CAFs (Fig. 6R). Similar results were obtained upon treatment of A549-MRC5 coculture by GPR77/CD10-targeted TAS/ICG nanoliposomes for 24 hours (Fig. 6S). The results were validated by flow cytometry where the combined TAS/ICG nanoliposomes demonstrated lower expression of those CAF markers compared to single TAS or ICG nanoliposomes (fig. S18).

Augmenting the antitumor efficacy of αPD-L1 via combination with dual nanoliposomes

CAFs have been implicated in limiting the efficacy of ICIs (*54*). We therefore tested whether the combined use of EpCAM-targeted SHK/GW exosome release inhibitory and/or GRP77/CD10-targeted TAS/ICG FGFR/β-catenin inhibitory nanoliposomes with αPD-L1 antibody results in a greater antitumor effect than αPD-L1 alone in vivo using the aggressive LLC syngeneic C57BL/6 mice model. Using five cycles of treatment (Fig. 7A), the combination of SHK/GW nanoliposomes with αPD-L1 significantly resulted in 19.7-fold reduction of tumor volume relative to the vehicle-treated group, whereas treatment with αPD-L1 alone had limited efficacy (~2.5-fold reduction of tumor volume) (Fig. 7B). Similarly, the concomitant use of TAS-120 or ICG-001 or TAS/ICG nanoliposomes with αPD-L1 enhanced the antitumor efficacy. On the other hand, monotherapy using either drug-loaded nanoliposomes alone or αPD-L1 therapy alone showed lower tumor inhibitory effects compared to combined drug nanoliposomes/αPD-L1 therapy, revealing their synergistic antitumor efficacy (fig. S19, A and B). Last, the combination of the EpCAM-targeted SHK/GW and/or GRP77/CD10-targeted TAS/ICG nanoliposomes (N9) with αPD-L1 resulted in the highest tumor growth inhibitory effect among all the treatment groups, with an almost complete inhibition of tumor growth (about 94.9% reduction of tumor volume) compared to only 58.9% reduction of tumor volume in αPD-L1–treated mice relative to the vehicle-treated mice (Fig. 7B). The results of tumor growth suppression were confirmed by immunofluorescence staining of the tumor sections for activation markers of CAFs (αSMA, FAP, S100A4, and PDGFRα) and ECM markers (COL1A1 and fibronectin). The expression of all fibroblast activation and ECM markers in tumor tissue samples of combined nanoliposome-treated group (N9) was lower than vehicle-treated group (Fig. 7C). This reduction in abundance of CAFs in tumor tissues corroborates with the reduced expression of exosomal markers CD63 and TSG101 in tumors treated with the combination of the nanoliposomes (N9) compared to vehicle- and αPD-L1–treated tumors (Fig. 7D).

According to flow cytometric analysis of tumor tissues, the $CD45^{-}EpCAM^{-}CD24^{-}CD105^{+}$ $PDGFR\alpha^{+}$ CAFs were highly abundant in vehicle- (79.6%) and αPD-L1 (76.9%)–treated tumors, with no significant difference between the two groups. This indicates that treatment with αPD-L1 alone does not reduce the abundance of CAFs in TME. On the contrary, treatment with dual-drug exosome release inhibitory and CAF phenotype-reversal nanoliposomes reduced the abundance of CAFs to 57.1 and 66.8%, respectively. The combined use of both dual-payload nanoliposomes (N9) with αPD-L1 reduced CAFs in TME to 46.4% (Fig. 7E and fig. S20). Moreover, the intratumoral infiltration of cytotoxic $CD8^{+}$ T cells was increased with the combinations of the two dual-payload nanoliposomes (N9) (Fig. 7D). According to flow cytometric analysis, using the combined strategy (N9) increased the infiltration of $CD8^{+}$ T cells to 59.2% compared to 36.2% for αPD-L1 treatment (Fig. 7F and fig. S21).

We did not notice any remarkable change in body weight of all treated mice groups over the treatment period, revealing a favorable safety profile with the absence of notable drug toxicity at the doses used in our treatment approach (Fig. 8A). Compared to αPD-L1–treated group, in which 60% of the mice died within 30 days, coadministration of SHK/GW and TAS/ICG nanoliposomes with αPD-L1 therapy resulted in 100% survival rate in our observation period of 50 days (Fig. 8B). In comparison, all the vehicle-treated mice died within 30 days of tumor inoculation.

CAFs are the major cells responsible for secretion of ECM proteins such as collagen and fibronectin, which form fibrous stromal barrier that physically hinders immune cell infiltration. Masson's trichrome staining of tumor tissues of αPD-L1– and dual-payload nanoliposome (N9)–treated mice showed 1.4- and 4.8-fold reduction in the deposition of collagen fibers compared to the vehicle-treated tumor tissues (Fig. 8C). This decrease in collagen deposition in tumor tissue is a consequence of the reduced abundance of CAFs by using our dual strategy. In addition to their stromal barrier function, CAFs generate immunosuppressive TME via secretion of factors such as SDF1 (CXCL12), CXCL13, TGFβ1, and Arginase 1, which reduce the activity of cytotoxic T lymphocytes and hence limit the antitumor efficacy of αPD-L1 immunotherapy. In the in vitro studies, the normalized fibroblasts showed reduced secretion of those immunosuppressive factors compared to activated CAFs. Moreover, CAFs, via secreting CXCL12 and other cytokines, stimulate the intratumoral infiltration of the immunosuppressive T_{regs} and M2 tumor-associated

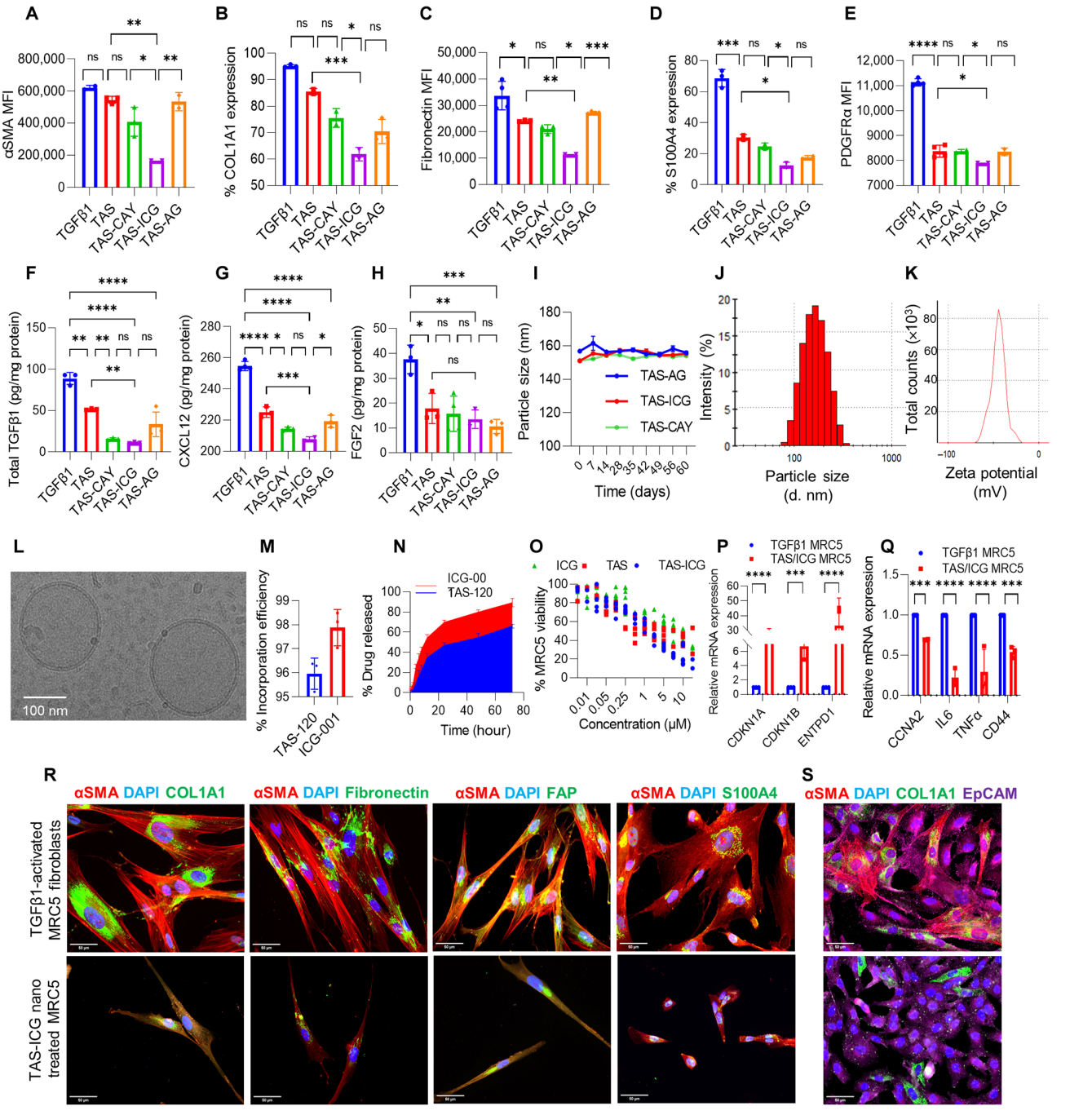

Fig. 6. CAF-targeted dual payload nanoliposomes reverse activated CAFs into a quiescent phenotype. Flow cytometry analysis of TGFβ1 pre-activated MRC5 fibroblasts treated with GPR77/CD10-targeted nanoliposomes for 24 hours showing the expression of fibroblast and ECM activation markers: (**A**) αSMA, (**B**) COL1A1, (**C**) fibronectin, (**D**) S100A4, and (**E**) PDGFRα. Data are shown as means ± SD ($n = 3$, $^{*}P < 0.05$, $^{**}P < 0.01$, $^{***}P < 0.001$, and $^{****}P < 0.0001$, ANOVA followed by Bonferroni's post hoc test). Secretory profile of TGFβ1 preactivated MRC5 fibroblasts treated with nanoliposomes for 24 hours compared to nontreated cells followed by ELISA of (**F**) TGFβ1, (**G**) CXCL12, and (**H**) FGF2. Data are shown as means ± SD ($n = 3$, $^{*}P < 0.05$, $^{**}P < 0.01$, $^{***}P < 0.001$, and $^{****}P < 0.0001$, ANOVA followed by Bonferroni's post hoc test). (**I**) Physical stability of nanoliposomes measured as particle size change upon storage at 4°C. (**J**) Particle size distribution of TAS/ICG nanoliposomes measured by dynamic light scattering. (**K**) Zeta potential of TAS/ICG nanoliposomes. (**L**) Cryo-TEM of TAS/ICG nanoliposomes. (**M**) Drug incorporation and (**N**) release from TAS/ICG nanoliposomes in PBS pH 7.4 at 37°C. (**O**) CCK8 viability of MRC5 fibroblasts treated with TAS/ICG nanoliposomes for 24 hours at 37°C CO_2 incubator. (**P** and **Q**) Relative mRNA expression of quiescence, proliferation, and stemness markers in MRC5 lung fibroblasts preactivated using TGFβ1 (10 ng/ml) for 24 hours and then treated with TAS/ICG nanoliposomes for 24 hours followed by qRT-PCR analysis. Data are shown as means ± SD ($n = 3$, $^{***}P < 0.001$ and $^{****}P < 0.0001$, ANOVA followed by Bonferroni's post hoc test). (**R**) Immunofluorescence imaging of MRC5 lung fibroblasts preactivated using TGFβ1 (10 ng/ml) for 24 hours and then treated with TAS/ICG nanoliposomes for 24 hours. Scale bars, 50 μm. (**S**) Immunofluorescence imaging of MRC5 fibroblasts directly cocultured with A549 cancer cells (1:1) and then treated with TAS/ICG nanoliposomes for 24 hours. Scale bars, 50 μm.

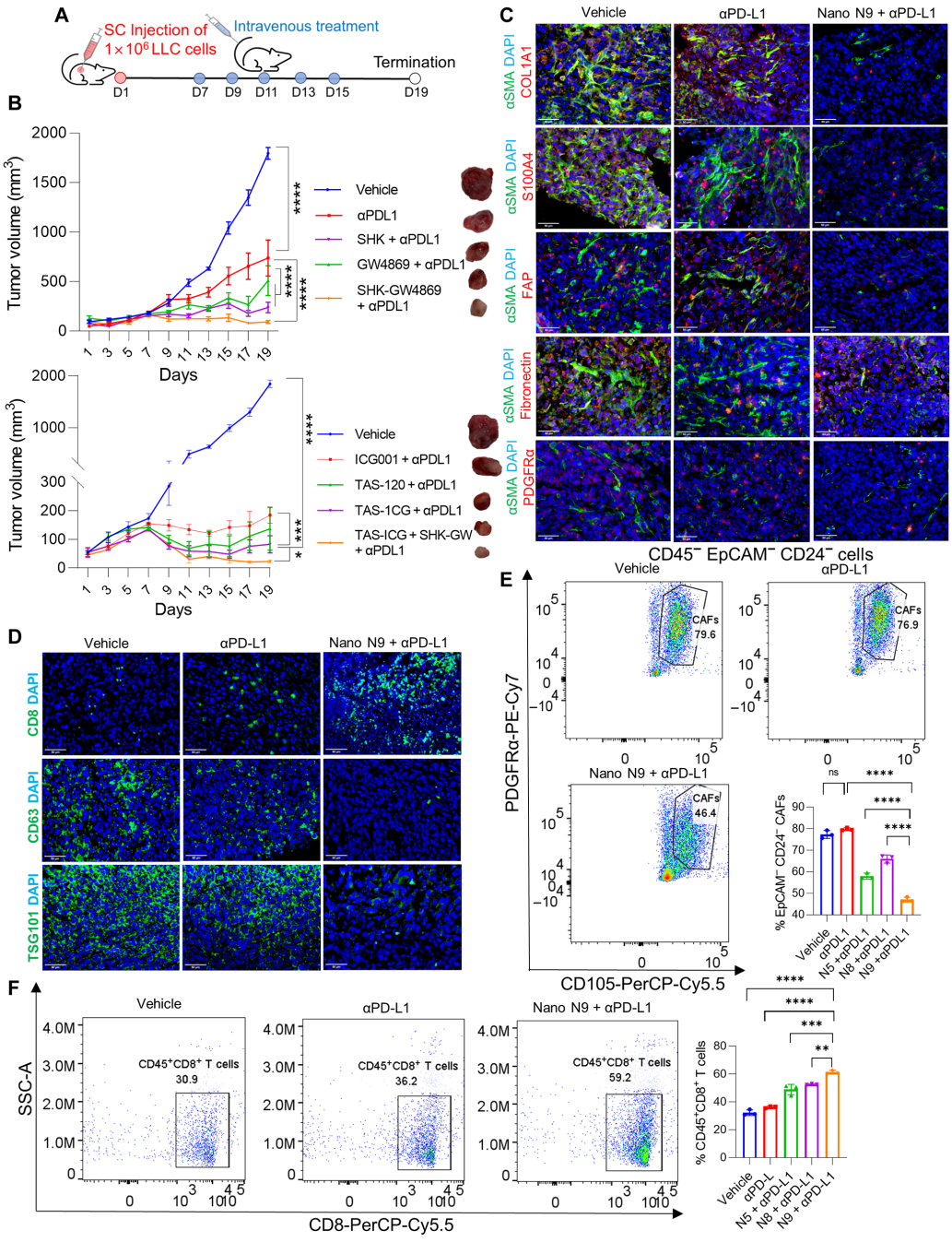

Fig. 7. Combination of CAF-modulating dual-payload nanoliposomes enhances antitumor efficacy of αPD-L1 in LLC syngeneic C57BL/6 mice. (**A**) Subcutaneous inoculation of 1x10^6 LLC cells into syngeneic C57BL/6 mice to induce tumor. (**B**) Tumor growth curves and representative images of tumors show the effect of different multidose treatments on tumor volume in LLC tumor-bearing mice. Each animal was injected into the tail vein with five doses of vehicle (control), αPD-L1 at a dose of 200 μg per mouse (10 mg/kg), single or combined EpCAM-targeted SHK/GW nanoliposomes (at equivalent dose of 0.4 and 0.75 mg/kg for SHK and GW, respectively), and single or combined GPR77/CD10-targeted TAS/ICG nanoliposomes (at equivalent dose of 1 and 2 mg/kg for TAS and ICG, respectively) on days 7, 9, 11, 13, and 15 after inoculation. Data shown are mean tumor volume ± SEM ($n = 5$, *$P < 0.05$, ***$P < 0.001$, and ****$P < 0.0001$, ANOVA followed by Bonferroni's post hoc test). Immunofluorescence imaging of tumor tissues isolated from LLC mice treated with vehicle, αPD-L1, and dual SHK/GW and TAS/ICG nanoliposomes (N9) + αPD-L1 shows the expression of (**C**) CAF activation and ECM markers and (**D**) CD8 and exosomal markers (CD63 and TSG101). Immunophenotyping analysis showing (**E**) abundance of CAFs (PDGFRα$^+$ CD105$^+$). Graph shows means ± SD ($n = 3$, ****$P < 0.0001$, ANOVA followed by Bonferroni's post hoc test). (**F**) Infiltration of effector T cells (CD45$^+$CD8$^+$), quantified using flow cytometry. Graph shows means ± SD ($n = 3$, **$P < 0.01$, ***$P < 0.001$, and ****$P < 0.0001$, ANOVA followed by Bonferroni's post hoc test). Tumors were harvested on day 19 after inoculation, and single-cell suspensions were prepared. N5, anti-EpCAM–targeted SHK/GW nanoliposomes; N8, anti-GPR77/CD10–targeted ICG/TAS nanoliposomes; N9, anti-EpCAM–targeted SHK/GW nanoliposomes + anti-GPR77/CD10–targeted ICG/TAS nanoliposomes. PE, phycoerythrin; PerCP, Peridinin-Chlorophyll-Protein.

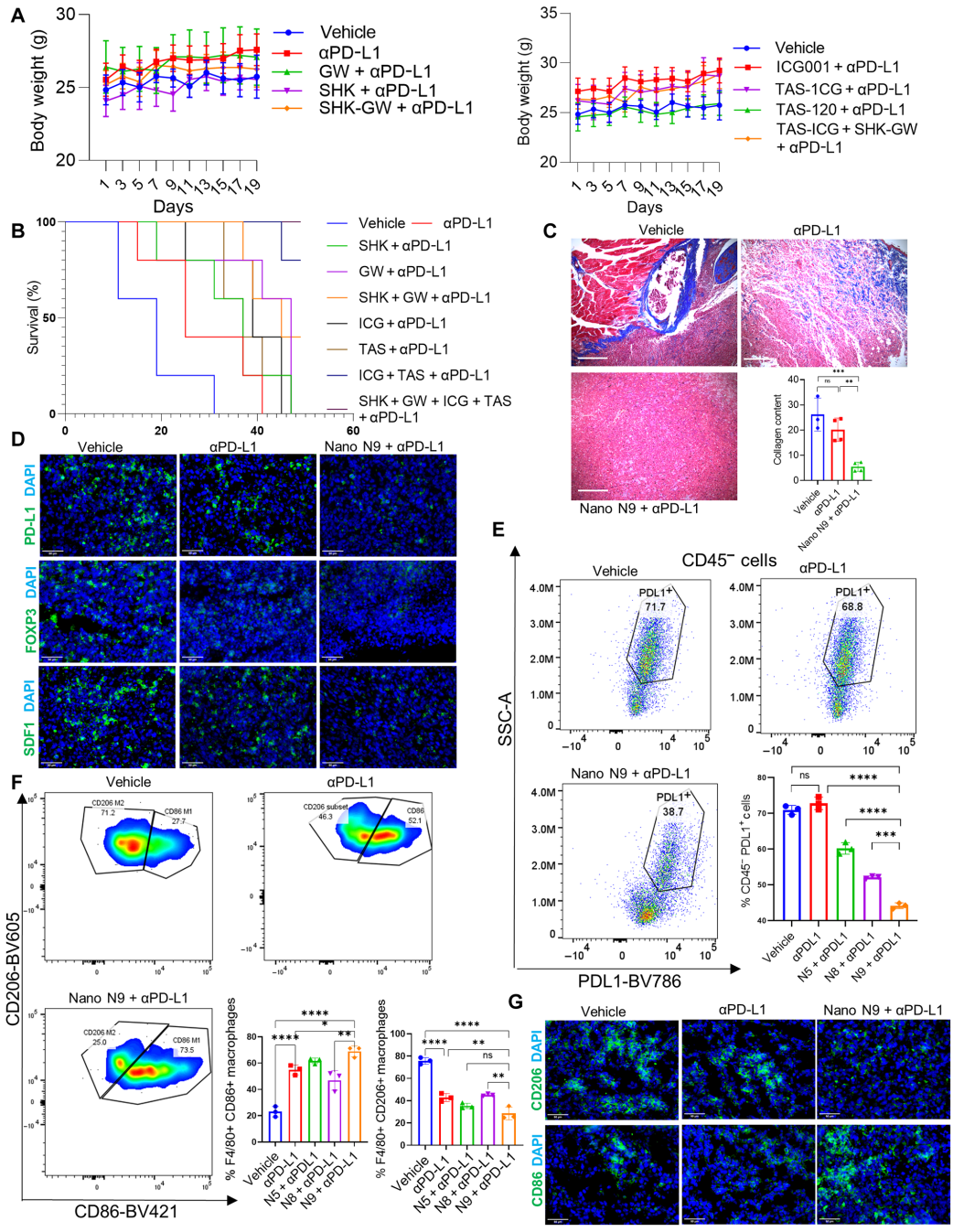

Fig. 8. CAF-modulating dual-payload nanoliposomes show favorable safety profile and prolong survival of LLC syngeneic mice. (**A**) Drug safety of SHK/GW and TAS/ICG nanoliposomes assessed by measurement of overall body weight. Data shown are means ± SEM (n = 5). (**B**) Survival rate of mice treated with vehicle (control), αPD-L1 at a dose of 200 μg pe mouse (10 mg/kg), single or combined EpCAM-targeted SHK/GW nanoliposomes (at equivalent dose of 0.4 and 0.75 mg/kg for SHK and GW, respectively), or single or combined GPR77/CD10-targeted TAS/ICG nanoliposomes (at equivalent dose of 1 and 2 mg/kg for TAS and ICG, respectively) on days 7, 9, 11, 13, and 15 after inoculation. Data shown are mean ± SEM (n = 5). (**C**) Masson's Trichrome staining of tumor tissues isolated from LLC mice treated with vehicle, αPD-L1, and dual SHK/GW and TAS/ICG nanoliposomes (N9) + αPD-L1 illustrated as imaging of paraffin embedded tumor tissues. Scale bars, 500 μm. Graph shows quantification of collagen in tumor tissues. Data are shown as means ± SD (n = 3 to 4, $^{**}P < 0.0001$, ANOVA followed by Bonferroni's post hoc test). (**D**) Immunofluorescence imaging of tumor tissues isolated from LLC mice treated with vehicle, αPD-L1, and dual SHK/GW and TAS/ICG nanoliposomes (N9) + αPD-L1 shows the expression of immunosuppressive markers PD-L1 and SDF1 as well as T_{reg} cell marker (FOXP3). Immunophenotyping analysis showing (**E**) PD-L1 expression and (**F**) infiltration of M2 ($CD206^+$) and M1 ($CD86^+$) macrophages in tumor tissues isolated from LLC mice. Graphs show means ± SD (n = 3, $^{*}P < 0.05$, $^{***}P < 0.001$, $^{****}P < 0.0001$, ANOVA followed by Bonferroni's post hoc test). Tumors were harvested on day 19 after inoculation, and single-cell suspensions were prepared. (**G**) Immunofluorescence imaging of tumor tissues shows the infiltration of M2 ($CD206^+$) and M1 ($CD86^+$) macrophages. N5, anti-EpCAM–targeted SHK/GW nanoliposomes; N8, anti-GPR77/CD10–targeted ICG/TAS nanoliposomes; N9, anti-EpCAM–targeted SHK/GW nanoliposomes + anti-GPR77/CD10–targeted ICG/TAS nanoliposomes.

macrophages (*55*, *56*). Nanoliposome-treatment of tumor tissues reduced the expression of SDF-1 (CXCL12) and FOXP3, markers of the T_{reg} cells, relative to vehicle and αPD-L1 treatments (Fig. 8D). Treatment with nanoliposomes also reduced the expression of the T cell inhibitory marker Programmed Cell Death Protein 1 (PD-1) while enhancing the expression of inducible T cell costimulator (ICOS) compared to the vehicle- and αPD-L1–treated group. The apoptosis denoted by Caspase 3 was significantly higher in tumor tissues treated by nanoliposomes/αPD-L1 combination compared to αPD-L1– or vehicle-treated mice. On the contrary, Ki67 staining indicated reduced proliferation of tumor treated by the combined nanoliposomes compared to vehicle-treated mice (fig. S22). Those results reveal that the immunosuppressive nature of the TME could be reversed by our combined nanoliposomes treatment strategy that induce quiescence of CAFs with consequently decreased recruitment of immunosuppressive cells and increased infiltration of cytotoxic $CD8^+$ T cells. This explains the synergistic antitumor efficacy achieved by the combined use of nanoliposomes (N9) and αPD-L1 treatments.

Another mechanism that adds to the CAFs normalizing effect by the nanoliposomes is the reduced expression of PD-L1 in TME. Treatment with nanoliposomes reduced the expression of PD-L1 in TME to 38.7% for combined nanoliposomes (N9) compared to 71.7 and 68.8% for vehicle and αPD-L1 treatments, respectively (Fig. 8E and fig. S23). This was also confirmed by the results of immunofluorescence imaging (Fig. 8D). CAF-secreted CXCL12 has been reported to increase the PD-L1 expression in lung adenocarcinoma cells A549, PC-9, and H1975 (*57*), and blocking of FGFR also can reduce the expression of PD-L1 in lung cancer cells (*58*, *59*). Moreover, the intratumoral infiltration of protumoral $CD206^+$ M2 macrophages was reduced, while that of $CD86^+$ M1 antitumoral macrophages was increased in combined nanoliposome (N9)–treated tumors compared to vehicle and αPD-L1 treatments (Fig. 8, F and G). These findings are matching with in vitro studies where the quiescent fibroblasts promoted polarization of THP-1 macrophages to M1 phenotype.

DISCUSSION

The intricate cross-talk between cancer cells and CAFs within the TME is crucial in promoting immunosuppression, which, in turn, undermines the efficacy of ICIs. Therefore, there is an urgent need to inhibit activation of resident stromal fibroblasts into CAFs. Using a physical approach, Zhou *et al.* (*60*) suppressed the prometastatic role of fibroblasts by inhibiting their activation in distant organs. The tumor up-regulated matrix metalloproteinase 2 was exploited to cleave the peptide FR17 to form a lamellar structure "nano-blanket." The nano-blanket wrapped the surface of fibroblasts acting as a physical shield to inhibit their activation by tumor-derived factors. Administration of FR17 peptide into B16F10 melanoma lung metastasis mouse model effectively inhibited the formation of pulmonary premetastatic niche and metastasis. Moreover, because of the high heterogeneity of CAFs, an efficient strategy that can inhibit activation of fibroblasts originating from different sources is required. Cancer cell–derived exosomes not only are involved in the differentiation of resident fibroblasts but also contribute to transdifferentiation of endothelial cells, epithelial cells (*61*–*63*), bone marrow–derived MSCs (*64*), and pericytes into CAFs (*65*). Therefore, we anticipate that suppressing the release of tumoral exosomes is a promising approach that can inhibit induction of activated CAF phenotypes from different cell origins.

Exosome biogenesis starts within the endosomal system where inward invagination of the limiting membrane of the endosome to give rise to intraluminal vesicles (ILVs) defines the maturation of the early endosome into late endosome, called the MVB (*66*). Multiple steps and pathways are implicated in exosome biogenesis. For example, the early steps involve the neutral sphingomyelinase-mediated synthesis of ceramide, which coalesce into raft-based microdomains to promote the inward invagination or budding of the membrane (*67*). In addition, small guanosine triphosphatase (GTPase) ARF6 (ARF) and its effector phospholipase D2 can regulate syntenin that regulates budding of ILVs into MVBs. These MVBs are then trafficked to the plasma membrane via interactions with cytoskeletal proteins, which is primarily mediated by Rab GTPases (*68*). The fusion of the MVBs with the plasma membrane, mediated by the SNARE complex, enables the release of the exosomes into the extracellular environment (*66*, *68*).

We therefore engineered nanoliposomes encapsulating molecular inhibitors of different steps implicated in exosome biogenesis, which resulted in suppression of exosome release from lung cancer cells. This, in turn, inhibited the differentiation of lung fibroblasts into CAFs. Among all inhibitors tested, the combined SHK/GW nanoliposomes demonstrated superior ability to suppress the exosome release and fibroblast activation via synergistic inhibition of MVB and SNARE complex formation. The SHK/GW nanoliposomes reduced the release of all exosome phenotypes particularly $CD9^+$ exosomes from lung cancer cells. CD9 is a tetraspanin commonly found on the surface of exosomes and has been implicated in cell adhesion, migration, and metastasis of cancer cells (*69*). Dimitrakopoulos *et al.* (*70*) shows that $CD9^+$ plasma exosomes are increased in patients with lung cancer in comparison to healthy controls, while lower levels of $CD9^+$ exosomes have been detected after chemotherapy, suggesting a prognostic value. Moreover, $CD9^+$ exosomes have been shown to facilitate tumor-stroma cross-talk, including fibroblasts (*69*, *71*). According to our observations, $CD9^+$ exosomes may play a role in promoting a protumorigenic TME by aiding the reprogramming of fibroblasts to CAFs. Our findings indicate a reduced release of exosomes, particularly $CD9^+$ ones, from lung cancer cells treated with our SHK/GW nanoliposomes. This suggests that our therapeutic strategy potentially interferes with the exosome-mediated communication pathways essential for tumor progression. Furthermore, the enrichment of $CD9^+$ exosomes in nontreated lung cancer cells may suggest a potential biomarker role for $CD9^+$ exosomes in lung cancer progression.

EpCAM is up-regulated on lung cancer cells and undergoes internalization and recycling (*72*, *73*), which is critical for targeted drug delivery. Therefore, decoration of liposomal surface with anti-EpCAM antibodies further enhanced their lung cancer cell targeting. This, in turn, increases drug accumulation in cancer cells, resulting in enhanced therapeutic efficacy and maximal inhibition of release of tumoral exosomes.

Our study primarily focused on shifting CAFs from a protumorigenic and immunosuppressive state to a more quiescent state to alleviate immunosuppression and enhance the efficacy of ICIs. While our research did not explicitly explore the induction of an antitumorigenic phenotype in CAFs, we observed a significant reduction in the migration and invasive ability of cancer cells, promoted macrophage polarization to M1 antitumoral phenotype, and enhanced the activity of $CD8^+$ T cells. These findings suggest that our strategy may have potential to reverse CAFs to antitumoral phenotype not only a quiescent one. This can be explained by the ability of exosome release inhibitory nanoliposomes to change the fibroblast secretome

and gene expression profile, resulting in reduced secretion of TGFβ1, CXCL12, and FGF2 and down-regulation of proliferation, immunosuppression, and stemness markers. Collectively, our exosome release inhibitory strategy could maintain the fibroblasts in a quiescent phenotype, which, in turn, could reduce their tumorigenic and immunosuppressive functions. These results demonstrate the ability of SHK/GW nanoliposomes to weaken the cross-talk between CAFs with cancer cells, macrophages, and cytotoxic T lymphocytes in the TME. To further elucidate whether our strategy can promote an antitumorigenic phenotype in CAFs, future additional studies that would involve a more detailed phenotypic and functional characterization of CAFs after treatment will be needed.

While the exosome-inhibitory nanoliposomes prevent the generation of new CAFs, it is imperative to switch the activated phenotype of pre-existing CAFs into quiescent one. Nanomedicines have been previously used to reprogram CAFs by interfering with TGFβ-induced fibroblast differentiation via delivery of TGFβ inhibitors such as relaxin-2 (*74*), α-mangostin (*75*), and fraxinellone (*76*). The nanoparticles successfully inactivated CAFs as denoted by reduced expression of αSMA and collagen. In another approach, hydroxychloroquine liposomes could inhibit autophagy-mediated activation of pancreatic stellate cells into CAFs (*77*). This consequently enhanced the cytotoxicity of the coloaded paclitaxel against pancreatic cancer cells. Furthermore, other types of nanomedicines have been investigated as potential CAF deactivators by down-regulating ROS in the TME (*78*), hypoxia inhibition (*79*), stimulating vitamin D receptor (*80*), or regulating lipid metabolism (*81*).

Among the various signaling inhibitors investigated in our study, the combined TAS-120/ICG-001 nanoliposomes resulted in the most efficient quiescence of TGFβ1-activated lung fibroblasts via blockage of the up-regulated FGFR and Wnt/β-catenin axes in CAFs, respectively. This was evidenced by marked down-regulation of CAF activation and ECM markers. This combination is consistent with the reported cross-talk between the FGF and β-catenin signaling pathways where FGF, via binding to FGFR, was found to enhance proliferation of cells via AKT-induced β-catenin activation and CBP/β-catenin–mediated transcription (*82*). In many cancer types, FGFR was found to facilitate Wnt/β-catenin pathway; for example, FGFR4 was reported to enhance CAF-mediated epithelial-mesenchymal transition in colorectal cancer cells through activation of β-catenin pathway (*83*, *84*). Active targeting is a promising approach to enhance the selectivity of nanoliposomes and increase drug accumulation at the specific cell target. The commonly used CAF markers such as α-SMA and FAP characterize different cell populations that show distinct expression profiles, revealing a strong degree of heterogeneity of CAFs (*85*). Therefore, targeting α-SMA$^+$ or FAP$^+$ CAF populations is nonspecific and targets different populations of CAFs that may cause contradicting results. Therefore, because of the pleiotropic functions and heterogenous subsets of CAFs, we targeted a specific subset of tumorigenic and stemness-promoting CAFs (GPR77$^+$CD10$^+$ CAFs) rather than targeting the other CAF subsets. As a result, the GPR77/CD10-targeted TAS/ICG nanoliposomes efficiently induced quiescence of CAFs, resulting in up-regulation of quiescence markers together with impaired tumorigenic and immunosuppressive functions.

In addition to the challenge of CAFs' heterogeneity, the high plasticity CAFs, ability to dynamically change their phenotype in response to different TME signals, represents another challenge for anticancer therapies (*86*, *87*). Our dual-therapeutic approach is not only focused on inducing quiescence of CAFs but also can mitigate the dynamic nature of CAFs by simultaneously targeting multiple components of the TME that contribute to CAF plasticity. First, modulating tumoral exosome release aims to disrupt the communication between cancer cells and fibroblasts within TME. Therefore, we hypothesize that our SHK/GW ERI nanoliposomes could stabilize CAFs in a more quiescent state, reducing their phenotypic plasticity. In parallel, by targeted inhibition of FGFR-Wnt/β-catenin signaling axes in GPR77$^+$CD10$^+$ CAFs, critical pathways involved in the activation and maintenance of the CAF phenotype, our TAS/ICG nanoliposomes address not only the heterogeneity of CAFs but also their ability to transition between different activation states. This could potentially limit the dynamic range of CAF plasticity.

Upon administration into LLC syngeneic lung cancer–bearing mice, the combination of exosome release inhibitory and FGFR/β-catenin inhibitory nanoliposomes with αPD-L1 immunotherapy resulted in the highest antitumor efficacy with almost complete tumor regression among the treated groups. In our study, we used SHK and GW at doses of 0.4 and 0.75 mg/kg, respectively, lower than their reported cytotoxic doses [1 to 10 mg/kg and 1.25 to 2.5 mg/kg, respectively (*88*, *89*)] in combination with αPD-L1 at a dose of 200 μg per mouse (10 mg/kg) each alternate day. Therefore, we assume that their tumor growth inhibitory effect is mediated via inhibition of tumoral exosome release, which, in turn, reduces activation of fibroblasts in the TME and hence decrease their immunosuppressive functions. In parallel, we used TAS-120 and ICG-001 at doses of 1 and 2 mg/kg, respectively, much lower than their reported anticancer doses [TAS-120; 25 mg/kg orally daily for 14 days (*90*); ICG-001; 5 mg/kg orally daily for 10 days (*91*)] to reverse the activated phenotype of CAFs via blocking of two major signaling pathways responsible for maintaining the activated CAFs phenotype.

Collectively, reduction of CAFs' abundance in the TME in combination with αPD-L1 therapy could efficiently reduce tumor burden and prolong the survival of lung cancer bearing mice. Mechanistically, the dual-payload nanoliposome-mediated quiescence of CAFs reversed the immunosuppressive TME via multifaceted approach. First, the stromal barrier was relieved due to reduced secretion of ECM proteins (e.g., collagen), which enhances immune cell infiltration. Second, reprogramming of CAFs reduced the secretion of immunosuppressive mediators such as PD-L1, TGFβ1, and CXCL12. Those factors inhibit the activity and infiltration of CTLs while enhancing recruitment of immunosuppressive cells. Third, the infiltration of immunosuppressive cells, e.g., T_{regs} and M2 macrophages into the tumor, has been reduced. CAFs are known to secrete the chemokines CCL22 and CCL2 that attract T_{regs} and M2 macrophages to the TME (*92*). Therefore, normalization of CAFs changes its secretory function and hence reduces chemoattraction of T_{regs} and M2 macrophages while promoting polarization to M1 phenotype. Last, consequently, the intratumoral infiltration of cytotoxic CD8$^+$ T cells has been increased. Moreover, the up-regulated ICOS, a member of CD28 superfamily, by T cells indicates their costimulation and proliferation where ICOS promotes T helper 1 (T_H1) and T_H17 responses, leading to strong antitumor immune response. In contrast, the expression of the T cell inhibitory receptor PD-1 has been down-regulated, which, in turn, reverses T cell exhaustion and amplify their antitumor activity. The effect of modulating CAFs on the expression of ICOS and PD-1 can be mediated by alteration of the secretion pattern of cytokines and chemokines.

In summary, our proposed treatment strategy rationalizes the modulation of CAFs as a tool to reverse the immunosuppressive TME to immune-competent one. The programming of CAFs into quiescent fibroblasts has been a holy grail in cancer medicine but has been a substantial hurdle to cross. Our results indicate that a two-step

process—first, shutting down tumoral exosome biogenesis and release—could inhibit the transdifferentiation of fibroblasts into CAFs and—second, perturbing the pathways that sustain the activated CAF state—can restore the quiescent phenotype of activated CAFs. This is a comprehensive study, where we have screened multiple nanoliposomes with payloads that target different molecular targets mediating the above processes. However, our results suggest that each step is better achieved by combining two distinct molecular-targeted payloads in one liposome. Recent clinical studies have revealed that the combination of two drugs in a nanoparticle resulted in a greater antitumor efficacy compared to the combination of the same drugs administered in the classical formulations (*93*). Here, the need to inhibit at multiple levels of exosome biogenesis and release, and FGF signaling together with Wnt/β-catenin to perturb the existing CAFs indeed highlights the complexity of manipulating CAFs as a target and also the opportunity of harnessing nanoliposomes to address this challenging problem.

In this study, we suggest that the combined use of SHK/GW exosome release inhibitory and TAS/ICG FGFR/β-catenin blocking nanoliposomes is more effective in fibroblast normalization than single use of the individual nanoliposomes. First, SHK/GW nanoliposomes successfully suppressed the differentiation of normal fibroblasts into CAFs. However, they cannot induce quiescence of the already activated CAFs due to lack of antifibrotic activity. Similarly, TAS/ICG nanoliposomes successfully induced quiescence of activated CAFs. However, they cannot inhibit activation of fibroblasts. Multiple factors (e.g., TGFβ1, TNFα, FGF2, PDGF, and EGF) are involved in the fibroblast differentiation into CAFs. Therefore, suppressing the release of tumoral exosomes that contain multiple fibrogenic factors is more efficient to prevent fibroblast differentiation than blocking one or two signaling pathways. Overall, it is necessary to combine SHK/GW nanoliposomes with TAS/ICG ones to maintain a quiescent fibroblast phenotype.

A noteworthy finding in the current study is the augmentation of the efficacy of a PD-L1 ICI with the combinatorial nanoliposomes. Despite the promise of ICIs, only a subset of patients exhibit durable response (*94*). Improving outcomes with immune checkpoint inhibition has emerged as a major goal in cancer therapy (*95*). Our results validate the critical role that CAFs play in limiting the efficacy of immunotherapy (*96*). The treatment with combination nanoliposomes decreased the production of the immunosuppressive and protumorigenic mediators in TME; reduced the expression of PD-L1, PD-1, CXCL12, and FOXP3; increased the expression of stimulatory molecules such as ICOS; and increased the intratumoral infiltration of cytotoxic $CD8^+$ T lymphocytes, which can explain the increased antitumor efficacy when the ICI is combined with the CAF-modulating nanoliposomes. While we observed strong efficacy in animal studies, clinical translation will require the development of more selective inhibitors of the molecular targets. Our integrative strategy underpinned by CAF modulatory dual-drug nanoliposomes can emerge as a paradigm shift in the search for strategies to enhance the efficacy of cancer immunotherapy.

MATERIALS AND METHODS

Methods are presented in detail in the Supplementary Materials.

Engineering nanoliposomes

Drug payload [at typically 10 mol percent (mol %) unless specified], cholesterol(5mol%),1,2-distearoyl-*sn*-glycero-3-phosphoethanolamine-*N*-[carboxy(polyethylene glycol)-2000] (35 mol %), and l-α-phosphatidylcholine (50 mol %) were dissolved in 1-ml mixture of dichloromethane/methanol at 1:1 (v/v). The solvent was evaporated into a thin and uniform film using a rotary evaporator. The film was then hydrated with 1.0 ml of sterile PBS for 1.5 hours at 60°C. After hydration, one equivalent of 1-ethyl-3-(3-dimethylaminopropyl)carbodiimide and *N*-hydroxysuccinimide were each added and incubated at room temperature for 2 hours. To the samples, different concentrations (1, 4, 8, and 20, of 0.5 mg/kg concentration) of immunoglobulin G (control), anti-EpCAM antibodies, or anti-GPR77/anti-CD10 (1:1) were added and the samples were incubated at 4°C for 12 hours. After incubation, the samples were extruded at 60°C using a 400 nm and then a 200-nm PC membrane to prepare particles <200 nm. The samples were then more purified by passing through a Sephadex G-25 column to remove free molecular drugs and nonconjugated antibodies.

Physicochemical characterization

The drug incorporation efficiency in nanoliposomes was determined by using ultraviolet-visible spectroscopy. The hydrodynamic diameter and zeta potential of the liposomes were measured by dynamic light scattering using Zetasizer Nano ZS90 (Malvern, UK). The physical stability of the drug-loaded nanoliposomes was evaluated by measuring the particle size at predetermined time intervals during storage at 4°C. Morphological analysis of the nanoliposomes was carried out via cryo–transmission electron microscopy.

Testing in vitro

The binding and internalization of the nanoliposomes were assessed using fluorescence microscopy and flow cytometry, respectively, while their cytotoxicity to cancer cells and fibroblasts was tested using a CCK8 cell viability kit.

Exosome purification, characterization, and analysis

A549 lung cancer cells were cultured in F-12K media containing 10% fetal bovine serum until be 70 to 80% confluency. The cells were then treated with the exosome release inhibitory nanoliposomes for 24 hours. Then, the medium was replaced with fresh media containing 5% exosome-depleted FBS for 48 hours. The conditioned medium was centrifuged to 2000*g* for 30 min to remove cells and debris, supernatant was mixed with 0.5 volumes of the Total Exosome Isolation Reagent (Invitrogen), and exosomes were separated according to manufacturer's protocol and lastly resuspended in PBS. The total protein concentration of the isolated exosomes was measured using the BCA Protein Assay Kit (Pierce; Thermo Fisher Scientific). The exosomal particle concentration and size distribution were determined using NTA with a NanoSight NS300 (Malvern Instruments). The tetraspanin marker expressing exosomes were quantified using CD63 ExoELISA ULTRA kit and ExoFlow cytometry using magnetic DynaBeads. The exosome count was also determined via EXOCET colorimetric assay based on its cholinesterase activity. The phenotype of isolated exosomes was further analyzed via interferometric imaging using ExoView R100 reader (NanoView Biosciences, Boston, MA).

Testing the effect of exosome biogenesis and release-inhibitory nanoliposomes on generation of CAFs

MRC5 human lung fibroblasts were seeded in Dulbecco's modified Eagle's medium (DMEM) containing 10% FBS up to 50% confluency in 12-well glass bottom plate. The medium was then replaced with serum-free DMEM for 48 hours growth arrest.

Then, the fibroblasts were activated using different experimental designs including (i) direct coculture of fibroblasts with A549 lung cancer cell–derived exosomes, (ii) indirect coculture with A549 cell–released exosomes via Transwell culture insert system, (iii) coculture of fibroblasts with A549 cancer cell–generated CM, and (iv) direct coculture of fibroblasts with A549 cancer cells. The effect of nanoliposome treatment on activation of fibroblasts was then evaluated via immunofluorescence imaging and flow cytometry. The secretory profile of the fibroblasts was investigated using enzyme-linked immunosorbent assay (ELISA), while the gene expression was assessed using qRT-PCR. For testing the effect of treatment with exosome release inhibitory nanoliposomes on the cross-talk between CAFs and different TME cell populations including cancer cells, macrophages, and cytotoxic T lymphocytes, we carried out wound healing assay, invasion assay, macrophage polarization testing, and lastly investigating the in vitro cytotoxic T cell activity.

Testing FGFR/β-catenin–blocking nanoliposomes to induce reversal of activated CAFs

MRC5 lung fibroblasts were grown to 50% confluence, growth arrested for 48 hours, and then activated by adding human TGFβ1 (10 ng/ml) for 24 hours. The drug nanoliposomes were then added to the preactivated fibroblasts for 24 hours, followed by analysis of the fibroblast phenotype as previously described.

In vivo efficacy studies

LLC lung cancer cells (1×10^6) were implanted subcutaneously in the flanks of 8- to 10-week old C57BL/6 mice (weighing 25 g; Charles River Laboratories) to generate tumor bearing syngeneic mice model. The drug therapy was started when the tumor volume reached ~80 to 100 mm^3. The tumor-bearing mice were treated with drug therapy administered by intravenous tail-vain injection every alternate day for total of five dosages according to the schedule illustrated in table S5. The tumor volumes and body weights were monitored on every alternate day for 11 days after injection. The survival rate was also calculated. The tumor volume was calculated by using the formula, $L \times B^2/2$, where the longest diameter was considered as L and the shortest diameter as B measured using a Vernier caliper. The animals were euthanized when either the average tumor volume of the control exceeded 2000 mm^3 in the control group or the tumors were necrotic. The tumors were harvested immediately following euthanizing and processed for further analysis including flow cytometry analysis, hematoxylin and eosin staining, Masson's trichrome staining, and immunofluorescence imaging. All animal procedures were approved by the Brigham and Women's Hospital (BWH) Institutional Use and Care of Animals Committee.

Statistical analysis

GraphPad Prism 8.0 (GraphPad Software Inc.) was used for all statistical analysis. Comparison between two groups was performed with Student's t test. The difference in tumor volume in mice among treatment groups was analyzed using analysis of variance (ANOVA) followed by Bonferroni's post hoc test. All tests were two-tailed. In vitro data are expressed as means ± SD; in vivo data are expressed as means ± SEM. A P value of <0.05 was considered statistically significant. All data had at least three independent replicates. All pathological analysis was blinded.

Supplementary Materials

This PDF file includes:

Supplementary Text
Figs. S1 to S23
Tables S1 to S8

REFERENCES AND NOTES

1. K. Kingwell, Uncoupling resistance to cancer immunotherapy. *Nat. Rev. Drug Discov.* **18**, 171 (2019).
2. V. P. Chauhan, I. X. Chen, R. Tong, M. R. Ng, J. D. Martin, K. Naxerova, M. W. Wu, P. Huang, Y. Boucher, D. S. Kohane, R. Langer, R. K. Jain, Reprogramming the microenvironment with tumor-selective angiotensin blockers enhances cancer immunotherapy. *Proc. Natl. Acad. Sci. U.S.A.* **116**, 10674–10680 (2019).
3. X. Chen, E. Song, Turning foes to friends: Targeting cancer-associated fibroblasts. *Nat. Rev. Drug Discov.* **18**, 99–115 (2019).
4. B. A. Pereira, C. Vennin, M. Papanicolaou, C. R. Chambers, D. Herrmann, J. P. Morton, T. R. Cox, P. Timpson, CAF subpopulations: A new reservoir of stromal targets in pancreatic cancer. *Trends Cancer* **5**, 724–741 (2019).
5. B. C. Özdemir, T. Pentcheva-Hoang, J. L. Carstens, X. Zheng, C. C. Wu, T. R. Simpson, H. Laklai, H. Sugimoto, C. Kahlert, S. V. Novitskiy, A. De Jesus-Acosta, P. Sharma, P. Heidari, U. Mahmood, L. Chin, H. L. Moses, V. M. Weaver, A. Maitra, J. P. Allison, V. S. LeBleu, R. Kalluri, Depletion of carcinoma-associated fibroblasts and fibrosis induces immunosuppression and accelerates pancreas cancer with reduced survival. *Cancer Cell* **25**, 719–734 (2014).
6. Y. Sun, J. Campisi, C. Higano, T. M. Beer, P. Porter, I. Coleman, L. True, P. S. Nelson, Treatment-induced damage to the tumor microenvironment promotes prostate cancer therapy resistance through WNT16B. *Nat. Med.* **18**, 1359–1368 (2012).
7. J. Fang, L. Xiao, K. I. Joo, Y. Liu, C. Zhang, S. Liu, P. S. Conti, Z. Li, P. Wang, A potent immunotoxin targeting fibroblast activation protein for treatment of breast cancer in mice. *Int. J. Cancer* **138**, 1013–1023 (2016).
8. R.-D. Hofheinz, S.-E. al- Batran, F. Hartmann, G. Hartung, D. Jäger, C. Renner, P. Tanswell, U. Kunz, A. Amelsberg, H. Kuthan, G. Stehle, Stromal antigen targeting by a humanised monoclonal antibody: An early phase II trial of sibrotuzumab in patients with metastatic colorectal cancer. *Onkologie* **26**, 44–48 (2003).
9. J. P. Webber, L. K. Spary, A. J. Sanders, R. Chowdhury, W. G. Jiang, R. Steadman, J. Wymant, A. T. Jones, H. Kynaston, M. D. Mason, Z. Tabi, A. Clayton, Differentiation of tumour-promoting stromal myofibroblasts by cancer exosomes. *Oncogene* **34**, 290–302 (2015).
10. J. Webber, R. Steadman, M. D. Mason, Z. Tabi, A. Clayton, Cancer exosomes trigger fibroblast to myofibroblast differentiation. *Cancer Res.* **70**, 9621–9630 (2010).
11. T. Fang, H. Lv, G. Lv, T. Li, C. Wang, Q. Han, L. Yu, B. Su, L. Guo, S. Huang, D. Cao, L. Tang, S. Tang, M. Wu, W. Yang, H. Wang, Tumor-derived exosomal miR-1247-3p induces cancer-associated fibroblast activation to foster lung metastasis of liver cancer. *Nat. Commun.* **9**, 191 (2018).
12. C. Ringuette Goulet, G. Bernard, S. Tremblay, S. Chabaud, S. Bolduc, F. Pouliot, Exosomes induce fibroblast differentiation into cancer-associated fibroblasts through TGFβ signaling. *Mol. Cancer Res.* **16**, 1196–1204 (2018).
13. J. Albrengues, T. Bertero, E. Grasset, S. Bonan, M. Maiel, I. Bourget, C. Philippe, C. Herraiz Serrano, S. Benamar, O. Croce, V. Sanz-Moreno, G. Meneguzzi, C. C. Feral, G. Cristofari, C. Gaggioli, Epigenetic switch drives the conversion of fibroblasts into proinvasive cancer-associated fibroblasts. *Nat. Commun.* **6**, 10204 (2015).
14. A. Li, P. Chen, Y. Leng, J. Kang, Histone deacetylase 6 regulates the immunosuppressive properties of cancer-associated fibroblasts in breast cancer through the STAT3-COX2-dependent pathway. *Oncogene* **37**, 5952–5966 (2018).
15. Y. Wei, D. Wang, F. Jin, Z. Bian, L. Li, H. Liang, M. Li, L. Shi, C. Pan, D. Zhu, X. Chen, G. Hu, Y. Liu, C. Y. Zhang, K. Zen, Pyruvate kinase type M2 promotes tumour cell exosome release via phosphorylating synaptosome-associated protein 23. *Nat. Commun.* **8**, 14041 (2017).
16. H. Zhang, J. Lu, J. Liu, G. Zhang, A. Lu, Advances in the discovery of exosome inhibitors in cancer. *J. Enzyme Inhib. Med. Chem.* **35**, 1322–1330 (2020).
17. M. Catalano, L. O'Driscoll, Inhibiting extracellular vesicles formation and release: A review of EV inhibitors. *J. Extracell. Vesicles* **9**, 1703244 (2019).
18. A. Datta, H. Kim, L. McGee, A. E. Johnson, S. Talwar, J. Marugan, N. Southall, X. Hu, M. Lal, D. Mondal, M. Ferrer, A. B. Abdel-Mageed, High-throughput screening identified selective inhibitors of exosome biogenesis and secretion: A drug repurposing strategy for advanced cancer. *Sci. Rep.* **8**, 8161 (2018).
19. S. Shu, Y. Yang, C. L. Allen, O. Maguire, H. Minderman, A. Sen, M. J. Ciesielski, K. A. Collins, P. J. Bush, P. Singh, X. Wang, M. Morgan, J. Qu, R. B. Bankert, T. L. Whiteside, Y. Wu, M. S. Ernstoff, Metabolic reprogramming of stromal fibroblasts by melanoma exosome microRNA favours a pre-metastatic microenvironment. *Sci. Rep.* **8**, 12905 (2018).

20. W. Ye, X. Tang, Z. Yang, C. Liu, X. Zhang, J. Jin, J. Lyu, Plasma-derived exosomes contribute to inflammation via the TLR9-NF-κB pathway in chronic heart failure patients. *Mol. Immunol.* **87**, 114–121 (2017).
21. G. G. Daaboul, P. Gagni, L. Benussi, P. Bettotti, M. Ciani, M. Cretich, D. S. Freedman, R. Ghidoni, A. Y. Ozkumur, C. Piotto, D. Prosperi, B. Santini, M. S. Ünlü, M. Chiari, Digital detection of exosomes by interferometric imaging. *Sci. Rep.* **6**, 37246 (2016).
22. A. Gori, A. Romanato, B. Greta, A. Strada, P. Gagni, R. Frigerio, D. Brambilla, R. Vago, S. Galbiati, S. Picciolini, M. Bedoni, G. G. Daaboul, M. Chiari, M. Cretich, Membrane-binding peptides for extracellular vesicles on-chip analysis. *J. Extracell. Vesicles* **9**, 1751428 (2020).
23. H. Wang, L. Fu, D. Wei, B. Wang, C. Zhang, T. Zhu, Z. Ma, Z. Li, Y. Wu, G. Yu, MiR-29c-3p suppresses the migration, invasion and cell cycle in esophageal carcinoma via CCNA2/p53 axis. *Front. Bioeng. Biotechnol.* **8**, 75 (2020).
24. S. Busch, D. Andersson, E. Bom, C. Walsh, A. Ståhlberg, G. Landberg, Cellular organization and molecular differentiation model of breast cancer-associated fibroblasts. *Mol. Cancer* **16**, 73 (2017).
25. Y. Shintani, A. Fujiwara, T. Kimura, T. Kawamura, S. Funaki, M. Minami, M. Okumura, IL-6 secreted from cancer-associated fibroblasts mediates chemoresistance in NSCLC by increasing epithelial-mesenchymal transition signaling. *J. Thorac. Oncol.* **11**, 1482–1492 (2016).
26. T. Kato, K. Noma, T. Ohara, H. Kashima, Y. Katsura, H. Sato, S. Komoto, R. Katsube, T. Ninomiya, H. Tazawa, Y. Shirakawa, T. Fujiwara, Cancer-associated fibroblasts affect intratumoral $CD8^+$ and $FoxP3^+$ T cells Via IL6 in the tumor microenvironment. *Clin. Cancer Res.* **24**, 4820–4833 (2018).
27. H. Kasashima, A. Duran, A. Martinez-Ordoñez, Y. Nakanishi, H. Kinoshita, J. F. Linares, M. Reina-Campos, Y. Kudo, A. L'Hermitte, M. Yashiro, M. Ohira, F. Bao, D. V. F. Tauriello, E. Batlle, M. T. Diaz-Meco, J. Moscat, Stromal SOX2 upregulation promotes tumorigenesis through the generation of a SFRP1/2-expressing cancer-associated fibroblast population. *Dev. Cell* **56**, 95–110.e10 (2021).
28. Y. Kinugasa, T. Matsui, N. Takakura, CD44 expressed on cancer-associated fibroblasts is a functional molecule supporting the stemness and drug resistance of malignant cancer cells in the tumor microenvironment. *Stem Cells* **32**, 145–156 (2014).
29. X. Yang, Y. Li, L. Zou, Z. Zhu, Role of exosomes in crosstalk between cancer-associated fibroblasts and cancer cells. *Front. Oncol.* **9**, 356 (2019).
30. L. Monteran, N. Erez, The dark side of fibroblasts: Cancer-associated fibroblasts as mediators of immunosuppression in the tumor microenvironment. *Front. Immunol.* **10**, 1835 (2019).
31. L. Portella, A. M. Bello, S. Scala, CXCL12 signaling in the tumor microenvironment. *Adv. Exp. Med. Biol.* **1302**, 51–70 (2021).
32. A. Kulkarni, V. Chandrasekar, S. K. Natarajan, A. Ramesh, P. Pandey, J. Nirgud, H. Bhatnagar, D. Ashok, A. K. Ajay, S. Sengupta, A designer self-assembled supramolecule amplifies macrophage immune responses against aggressive cancer. *Nat. Biomed. Eng.* **2**, 589–599 (2018).
33. A. Zhang, Y. Qian, Z. Ye, H. Chen, H. Xie, L. Zhou, Y. Shen, S. Zheng, Cancer-associated fibroblasts promote M2 polarization of macrophages in pancreatic ductal adenocarcinoma. *Cancer Med.* **6**, 463–470 (2017).
34. L. Ziani, S. Chouaib, J. Thiery, Alteration of the antitumor immune response by cancer-associated fibroblasts. *Front. Immunol.* **9**, 414 (2018).
35. S. E. Kuzet, C. Gaggioli, Fibroblast activation in cancer: When seed fertilizes soil. *Cell Tissue Res.* **365**, 607–619 (2016).
36. R. Kato, K. Haratani, H. Hayashi, K. Sakai, H. Sakai, H. Kawakami, K. Tanaka, M. Takeda, K. Yonesaka, K. Nishio, K. Nakagawa, Nintedanib promotes antitumour immunity and shows antitumour activity in combination with PD-1 blockade in mice: Potential role of cancer-associated fibroblasts. *Br. J. Cancer* **124**, 914–924 (2021).
37. S. Cattin, L. Ramont, C. Rüegg, Characterization and in vivo validation of a three-dimensional multi-cellular culture model to study heterotypic interactions in colorectal cancer cell growth, invasion and metastasis. *Front. Bioeng. Biotechnol.* **6**, 97 (2018).
38. J. Zhang, S. Li, Y. Zhao, P. Ma, Y. Cao, C. Liu, X. Zhang, W. Wang, L. Chen, Y. Li, Cancer-associated fibroblasts promote the migration and invasion of gastric cancer cells via activating IL-17a/JAK2/STAT3 signaling. *Ann. Transl. Med.* **8**, 877 (2020).
39. T. Liu, L. Zhou, K. Yang, K. Iwasawa, A. L. Kadekaro, T. Takebe, T. Andl, Y. Zhang, The β-catenin/YAP signaling axis is a key regulator of melanoma-associated fibroblasts. *Signal Transduct. Target. Ther.* **4**, 63 (2019).
40. K. W. Lee, S. Y. Yeo, C. O. Sung, S. H. Kim, Twist1 is a key regulator of cancer-associated fibroblasts. *Cancer Res.* **75**, 73–85 (2015).
41. S.-Y. Yeo, K.-W. Lee, D. Shin, S. An, K.-H. Cho, S.-H. Kim, A positive feedback loop bi-stably activates fibroblasts. *Nat. Commun.* **9**, 3016 (2018).
42. P. K. Dhanyamraju, P. S. Holz, F. Finkernagel, V. Fendrich, M. Lauth, Histone deacetylase 6 represents a novel drug target in the oncogenic Hedgehog signaling pathway. *Mol. Cancer Ther.* **14**, 727–739 (2015).
43. S. Su, J. Chen, H. Yao, J. Liu, S. Yu, L. Lao, M. Wang, M. Luo, Y. Xing, F. Chen, D. Huang, J. Zhao, L. Yang, D. Liao, F. Su, M. Li, Q. Liu, E. Song, $CD10^+GPR77^+$ Cancer-Associated Fibroblasts Promote Cancer Formation and Chemoresistance by Sustaining Cancer Stemness. *Cell* **172**, 841–856.e16 (2018).
44. T. W. LeBien, R. T. McCormack, The common acute lymphoblastic leukemia antigen (CD10)--emancipation from a functional enigma. *Blood* **73**, 625–635 (1989).
45. E. M. De Francesco, A. H. Sims, M. Maggiolini, F. Sotgia, M. P. Lisanti, R. B. Clarke, GPER mediates the angiocrine actions induced by IGF1 through the HIF-1α/VEGF pathway in the breast tumor microenvironment. *Breast Cancer Res.* **19**, 129 (2017).
46. N. P. Gerard, B. Lu, P. Liu, S. Craig, Y. Fujiwara, S. Okinaga, C. Gerard, An anti-inflammatory function for the complement anaphylatoxin C5a-binding protein, C5L2. *J. Biol. Chem.* **280**, 39677–39680 (2005).
47. E. H. Bent, L. R. Millán-Barea, I. Zhuang, D. R. Goulet, J. Fröse, M. T. Hemann, Microenvironmental IL-6 inhibits anti-cancer immune responses generated by cytotoxic chemotherapy. *Nat. Commun.* **12**, 6218 (2021).
48. H. Tsukamoto, K. Fujieda, S. Senju, T. Ikeda, H. Oshiumi, Y. Nishimura, Immune-suppressive effects of interleukin-6 on T-cell-mediated anti-tumor immunity. *Cancer Sci.* **109**, 523–530 (2018).
49. J. Wu, F. X. Gao, C. Wang, M. Qin, F. Han, T. Xu, Z. Hu, Y. Long, X. M. He, X. Deng, D. L. Ren, T. Y. Dai, IL-6 and IL-8 secreted by tumour cells impair the function of NK cells via the STAT3 pathway in oesophageal squamous cell carcinoma. *J. Exp. Clin. Cancer Res.* **38**, 321 (2019).
50. J. Rodon, J. Perez, R. Kurzrock, Combining targeted therapies: Practical issues to consider at the bench and bedside. *Oncologist* **15**, 37–50 (2010).
51. D. J. Agorku, A. Langhammer, U. Heider, S. Wild, A. Bosio, O. Hardt, CD49b, CD87, and CD95 are markers for activated cancer-associated fibroblasts whereas CD39 marks quiescent normal fibroblasts in murine tumor models. *Front. Oncol.* **9**, 716 (2019).
52. Y. T. Lee, Y. J. Tan, M. Falasca, C. E. Oon, Cancer-associated fibroblasts: Epigenetic regulation and therapeutic intervention in breast cancer. *Cancers (Basel)* **12**, 2949 (2020).
53. C. Vennin, P. Mélénec, R. Rouet, M. Nobis, A. S. Cazet, K. J. Murphy, D. Herrmann, D. A. Reed, M. C. Lucas, S. C. Warren, Z. Elgundi, M. Pinese, G. Kalna, D. Roden, M. Samuel, A. Zaratzian, S. T. Grey, A. Da Silva, W. Leung, S. Mathivanan, Y. Wang, A. W. Braithwaite, D. Christ, A. Benda, A. Parkin, P. A. Phillips, J. M. Whitelock, A. J. Gill, O. J. Sansom, D. R. Croucher, B. L. Parker, M. Pajic, J. P. Morton, T. R. Cox, P. Timpson, CAF hierarchy driven by pancreatic cancer cell p53-status creates a pro-metastatic and chemoresistant environment via perlecan. *Nat. Commun.* **10**, 3637 (2019).
54. R. L. Barrett, E. Puré, Cancer-associated fibroblasts and their influence on tumor immunity and immunotherapy. *eLife* **9**, e57243 (2020).
55. B. Zhang, C. Wu, Z. Zhang, K. Yan, C. Li, Y. Li, L. Li, CXCL12 is associated with $FoxP3^+$ tumor-infiltrating lymphocytes and affects the survival of patients with oral squamous cell carcinoma. *Oncol. Lett.* **18**, 1099–1106 (2019).
56. A. Costa, Y. Kieffer, A. Scholer-Dahirel, F. Pelon, B. Bourachot, M. Cardon, P. Sirven, I. Magagna, L. Fuhrmann, C. Bernard, C. Bonneau, M. Kondratova, I. Kuperstein, A. Zinovyev, A. M. Givel, M. C. Parrini, V. Soumelis, A. Vincent-Salomon, F. Mechta-Grigoriou, Fibroblast heterogeneity and immunosuppressive environment in human breast cancer. *Cancer Cell* **33**, 463–479.e10 (2018).
57. C. Inoue, Y. Miki, R. Saito, S. Hata, J. Abe, I. Sato, Y. Okada, H. Sasano, PD-L1 induction by cancer-associated fibroblast-derived factors in lung adenocarcinoma cells. *Cancers (Basel)* **11**, 1257 (2019).
58. S. S. Akhand, Z. Liu, S. C. Purdy, A. Abdullah, H. Lin, G. M. Cresswell, T. L. Ratliff, M. Wendt, Pharmacologic inhibition of FGFR modulates the metastatic immune microenvironment and promotes response to immune checkpoint blockade. *Cancer Immunol. Res.* **8**, 1542–1553 (2020).
59. S. Palakurthi, M. Kuraguchi, S. J. Zacharek, E. Zudaire, W. Huang, D. M. Bonal, J. Liu, A. Dhaneshwar, K. DePeaux, M. R. Gowaski, D. Bailey, S. N. Regan, E. Ivanova, C. Ferrante, J. M. English, A. Khosla, A. H. Beck, J. A. Rytlewski, C. Sanders, S. Laquerre, M. A. Bittinger, P. T. Kirschmeier, K. Packman, P. A. Janne, C. Moy, K. K. Wong, R. I. Verona, M. V. Lorenzi, The combined effect of FGFR inhibition and PD-1 blockade promotes tumor-intrinsic induction of antitumor immunity. *Cancer Immunol. Res.* **7**, 1457–1471 (2019).
60. Y. Zhou, P. Ke, X. Bao, H. Wu, Y. Xia, Z. Zhang, H. Zhong, Q. Dai, L. Wu, T. Wang, M. Lin, Y. Li, X. Jiang, Q. Yang, Y. Lu, X. Zhong, M. Han, J. Gao, Peptide nano-blanket impedes fibroblasts activation and subsequent formation of pre-metastatic niche. *Nat. Commun.* **13**, 2906 (2022).
61. J. H. Yeon, H. E. Jeong, H. Seo, S. Cho, K. Kim, D. Na, S. Chung, J. Park, N. Choi, J. Y. Kang, Cancer-derived exosomes trigger endothelial to mesenchymal transition followed by the induction of cancer-associated fibroblasts. *Acta Biomater.* **76**, 146–153 (2018).
62. D. W. Greening, S. K. Gopal, R. A. Mathias, L. Liu, J. Sheng, H. J. Zhu, R. J. Simpson, Emerging roles of exosomes during epithelial-mesenchymal transition and cancer progression. *Semin. Cell Dev. Biol.* **40**, 60–71 (2015).
63. K. S. Visan, R. J. Lobb, A. Moller, The role of exosomes in the promotion of epithelial-to-mesenchymal transition and metastasis. *Front. Biosci. (Landmark Ed)* **25**, 1022–1057 (2020).

64. Y. Yang, J. Li, Y. Geng, Exosomes derived from chronic lymphocytic leukaemia cells transfer miR-146a to induce the transition of mesenchymal stromal cells into cancer-associated fibroblasts. *J. Biochem.* **168**, 491–498 (2020).
65. X. Ning, H. Zhang, C. Wang, X. Song, Exosomes released by gastric cancer cells induce transition of pericytes into cancer-associated fibroblasts. *Med. Sci. Monit.* **24**, 2350–2359 (2018).
66. V. S. LeBleu, R. Kalluri, A peek into cancer-associated fibroblasts: Origins, functions and translational impact. *Dis. Model. Mech.* **11**, dmm029447 (2018).
67. K. Trajkovic, C. Hsu, S. Chiantia, L. Rajendran, D. Wenzel, F. Wieland, P. Schwille, B. Brügger, M. Simons, Ceramide triggers budding of exosome vesicles into multivesicular endosomes. *Science* **319**, 1244–1247 (2008).
68. K. M. McAndrews, R. Kalluri, Mechanisms associated with biogenesis of exosomes in cancer. *Mol. Cancer* **18**, 52 (2019).
69. R. Ondruššek, B. Kvokačková, K. Kryštofová, S. Brychtová, K. Souček, J. Bouchal, Prognostic value and multifaceted roles of tetraspanin CD9 in cancer. *Front. Oncol.* **13**, 1140738 (2023).
70. F. I. Dimitrakopoulos, A. E. Kottorou, K. Rodgers, J. T. Sherwood, G. A. Koliou, B. Lee, A. Yang, J. R. Brahmer, S. B. Baylin, S. C. Yang, H. Orita, A. Hulbert, M. V. Brock, Clinical Significance of Plasma CD9-Positive Exosomes in HIV Seronegative and Seropositive Lung Cancer Patients. *Cancers (Basel)* **13**, 5193 (2021).
71. H. Hasan, I. S. Sohal, Z. Soto-Vargas, A. M. Byappanahalli, S. E. Humphrey, H. Kubo, S. Kitdumrongthum, S. Copeland, F. Tian, A. Chairoungdua, A. L. Kasinski, Extracellular vesicles released by non-small cell lung cancer cells drive invasion and permeability in non-tumorigenic lung epithelial cells. *Sci. Rep.* **12**, 972 (2022).
72. N. Stefan, P. Martin-Killias, S. Wyss-Stoeckle, A. Honegger, U. Zangemeister-Wittke, A. Plückthun, DARPins recognizing the tumor-associated antigen EpCAM selected by phage and ribosome display and engineered for multivalency. *J. Mol. Biol.* **413**, 826–843 (2011).
73. M. Alibolandi, M. Ramezani, K. Abnous, F. Sadeghi, F. Atyabi, M. Asouri, A. A. Ahmadi, F. Hadizadeh, In vitro and in vivo evaluation of therapy targeting epithelial-cell adhesion-molecule aptamers for non-small cell lung cancer. *J. Control. Release* **209**, 88–100 (2015).
74. D. F. Mardhian, G. Storm, R. Bansal, J. Prakash, Nano-targeted relaxin impairs fibrosis and tumor growth in pancreatic cancer and improves the efficacy of gemcitabine in vivo. *J. Control. Release* **290**, 1–10 (2018).
75. J. Feng, M. Xu, J. Wang, S. Zhou, Y. Liu, S. Liu, Y. Huang, Y. Chen, L. Chen, Q. Song, J. Gong, H. Lu, X. Gao, J. Chen, Sequential delivery of nanoformulated α-mangostin and triptolide overcomes permeation obstacles and improves therapeutic effects in pancreatic cancer. *Biomaterials* **241**, 119907 (2020).
76. Y. Pei, L. Chen, Y. Huang, J. Wang, J. Feng, M. Xu, Y. Chen, Q. Song, G. Jiang, X. Gu, Q. Zhang, X. Gao, J. Chen, Sequential targeting TGF-β signaling and KRAS mutation increases therapeutic efficacy in pancreatic cancer. *Small* **15**, e1900631 (2019).
77. X. Chen, Q. Yu, Y. Liu, Q. Sheng, K. Shi, Y. Wang, M. Li, Z. Zhang, Q. He, Synergistic cytotoxicity and co-autophagy inhibition in pancreatic tumor cells and cancer-associated fibroblasts by dual functional peptide-modified liposomes. *Acta Biomater.* **99**, 339–349 (2019).
78. H. Xu, M. Hu, M. Liu, S. An, K. Guan, M. Wang, L. Li, J. Zhang, J. Li, L. Huang, Nano-puerarin regulates tumor microenvironment and facilitates chemo- and immunotherapy in murine triple negative breast cancer model. *Biomaterials* **235**, 119769 (2020).
79. T. Fourniols, E. Bastien, A. Canevat, O. Feron, V. Préat, Inhibition of colorectal cancer-associated fibroblasts by lipid nanocapsules loaded with acriflavine or paclitaxel. *Int. J. Pharm.* **584**, 119337 (2020).
80. X. Li, T. Yong, Z. Wei, N. Bie, X. Zhang, G. Zhan, J. Li, J. Qin, J. Yu, B. Zhang, L. Gan, X. Yang, Reversing insufficient photothermal therapy-induced tumor relapse and metastasis by regulating cancer-associated fibroblasts. *Nat. Commun.* **13**, 2794 (2022).
81. M. N. Hossen, G. Rao, A. Dey, J. D. Robertson, R. Bhattacharya, P. Mukherjee, Gold nanoparticle transforms activated cancer-associated fibroblasts to quiescence. *ACS Appl. Mater. Interfaces* **11**, 26060–26068 (2019).
82. N. Mavila, D. James, S. Utley, N. Cu, O. Coblens, K. Mak, C. B. Rountree, M. Kahn, K. S. Wang, Fibroblast growth factor receptor-mediated activation of AKT-β-catenin-CBP pathway regulates survival and proliferation of murine hepatoblasts and hepatic tumor initiating stem cells. *PLOS ONE* **7**, e50401 (2012).
83. S. Feng, L. Zhou, E. Collins Nice, C. Huang, Fibroblast growth factor receptors: Multifactorial-contributors to tumor initiation and progression. *Histol. Histopathol.* **30**, 13–31 (2015).
84. R. Liu, J. Li, K. Xie, T. Zhang, Y. Lei, Y. Chen, L. Zhang, K. Huang, K. Wang, H. Wu, M. Wu, E. C. Nice, C. Huang, Y. Wei, FGFR4 promotes stroma-induced epithelial-to-mesenchymal transition in colorectal cancer. *Cancer Res.* **73**, 5926–5935 (2013).
85. M. Desbois, Y. Wang, Cancer-associated fibroblasts: Key players in shaping the tumor immune microenvironment. *Immunol. Rev.* **302**, 241–258 (2021).
86. Y. Xu, W. Li, S. Lin, B. Liu, P. Wu, L. Li, Fibroblast diversity and plasticity in the tumor microenvironment: Roles in immunity and relevant therapies. *Cell Commun. Signal* **21**, 234 (2023).
87. R. A. Glabman, P. L. Choyke, N. Sato, Cancer-associated fibroblasts: Tumorigenicity and targeting for cancer therapy. *Cancers (Basel)* **14**, 3906 (2022).
88. M. Poggio, T. Hu, C. C. Pai, B. Chu, C. D. Belair, A. Chang, E. Montabana, U. E. Lang, Q. Fu, L. Fong, R. Blelloch, Suppression of exosomal PD-L1 induces systemic anti-tumor immunity and memory. *Cell* **177**, 414–427.e13 (2019).
89. X. Zhao, Y. Zhu, J. Hu, L. Jiang, L. Li, S. Jia, K. Zen, Shikonin inhibits tumor growth in mice by suppressing pyruvate kinase M2-mediated aerobic glycolysis. *Sci. Rep.* **8**, 14517 (2018).
90. L. Goyal, L. Shi, L. Y. Liu, F. Fece de la Cruz, J. K. Lennerz, S. Raghavan, I. Leschiner, L. Elagina, G. Siravegna, R. W. S. Ng, P. Vu, K. C. Patra, S. K. Saha, R. N. Uppot, R. Arellano, S. Reyes, T. Sagara, S. Otsuki, B. Nadres, H. A. Shahzade, I. Dey-Guha, I. J. Fetter, I. Baiev, E. E. Van Seventer, J. E. Murphy, C. R. Ferrone, K. K. Tanabe, V. Deshpande, J. J. Harding, R. Yaeger, R. K. Kelley, A. Bardelli, A. J. Iafrate, W. C. Hahn, C. H. Benes, D. T. Ting, H. Hirai, G. Getz, D. Juric, A. X. Zhu, R. B. Corcoran, N. Bardeesy, TAS-120 overcomes resistance to ATP-competitive FGFR inhibitors in patients with FGFR2 fusion-positive intrahepatic cholangiocarcinoma. *Cancer Discov.* **9**, 1064–1079 (2019).
91. W. R. Henderson Jr., E. Y. Chi, X. Ye, C. Nguyen, Y. T. Tien, B. Zhou, Z. Borok, D. A. Knight, M. Kahn, Inhibition of Wnt/beta-catenin/CREB binding protein (CBP) signaling reverses pulmonary fibrosis. *Proc. Natl. Acad. Sci. U.S.A.* **107**, 14309–14314 (2010).
92. X. Mao, J. Xu, W. Wang, C. Liang, J. Hua, J. Liu, B. Zhang, Q. Meng, X. Yu, S. Shi, Crosstalk between cancer-associated fibroblasts and immune cells in the tumor microenvironment: New findings and future perspectives. *Mol. Cancer* **20**, 131 (2021).
93. J. E. Lancet, G. L. Uy, L. F. Newell, T. L. Lin, E. K. Ritchie, R. K. Stuart, S. A. Strickland, D. Hogge, S. R. Solomon, D. Bixby, J. E. Kolitz, G. J. Schiller, M. J. Wieduwilt, D. H. Ryan, S. Faderl, Y.-L. Chang, J. Cortes, Five-year final results of a phase III study of CPX-351 versus 7+3 in older adults with newly diagnosed high-risk/secondary AML. *J. Clin. Oncol.* **38**, 7510–7510 (2020).
94. J. Galon, D. Bruni, Approaches to treat immune hot, altered and cold tumours with combination immunotherapies. *Nat. Rev. Drug Discov.* **18**, 197–218 (2019).
95. G. Morad, B. A. Helmink, P. Sharma, J. A. Wargo, Hallmarks of response, resistance, and toxicity to immune checkpoint blockade. *Cell* **184**, 5309–5337 (2021).
96. R. Barrett, E. Puré, Cancer-associated fibroblasts: Key determinants of tumor immunity and immunotherapy. *Curr. Opin. Immunol.* **64**, 80–87 (2020).

Acknowledgments: We acknowledge support from Fulbright Scholar Program for granting a postdoctoral research fellowship to A. Elzoghby. We thank S. Sengupta from Engineering in Medicine Division at Brigham and Women's Hospital for providing research facilities. We also thank A. Raj Ghosh from Ragon Institute of Mass General, MIT, and Harvard for helping with flow cytometry analysis. **Funding:** This work was supported in part by BRIght Futures Prize (funding #128447) awarded to A. Elzoghby by Brigham Research Institute (BRI) at Brigham and Women's Hospital. **Author contributions:** Conceptualization: A.O.E. and M.S.F. Methodology: M.S.F., M.T.M., A.K., H.E.E., K.P.M., and A.O.E.. Investigation: A.O.E. Visualization: M.S.F., M.T.M., A.K., H.E.E., and K.P.M. Supervision: A.O.E. Writing—original draft: A.O.E. and M.S.F. Writing—review and editing: A.O.E. **Competing interests:** The authors declare that they have no competing interests. **Data and materials availability:** All data needed to evaluate the conclusions in the paper are present in the paper and/or the Supplementary Materials.

Submitted 5 September 2023
Accepted 25 January 2024
Published 28 February 2024
10.1126/sciadv.adk3074